ENHANCING THE MECHANICAL AND DURABILITY PROPERTIES OF CEMENT MORTARS BY USING ALUMINA NANOCOATING ON CARBON NANOFIBERS

A Thesis

presented to

the Faculty of the Graduate School

at the University of Missouri-Columbia

In Partial Fulfillment

of the Requirements for the Degree

Master of Civil and Environmental Engineering

---

by

Huda Jamal Noori Al Qader

Dr. Hani Salim, Thesis Supervisor

MAY 2021

The undersigned, appointed by the dean of the Graduate School, have examined the thesis entitled:

ENHANCING THE MECHANICAL AND DURABILITY PROPERTIES OF CEMENT MORTARS BY USING ALUMINA NANOCOATING ON CARBON NANOFIBERS

presented by Huda Al Qader,

a candidate for the degree of Master of Science,

and hereby certify that, in their opinion, it is worthy of acceptance.

Professor Hani Salim

Professor Yaw Adu-Gyamfi

Professor Yangchuan Xing

DEDICATION

To my great mom

To my love Ahmed

ACKNOWLEDGEMENTS

I would like to express my sincere acknowledgement to all people who supported me in this journey. First, my deepest gratitude is given to my adviser Dr. Hani Salim. It was a complete privilege and honor to work with him. I am thankful for his trust, generosity, encouragement, and support. His positivity motivates me to work hard. He will always remain a source of inspiration for me. Second, I give many thanks to Dr. Yangchuan Xing for his collaboration on this project and for providing all nanomaterials used in this work. I also would like to thank Dr. Xing for serving as a committee member. Thanks for his student Dr. Ahmed Jasim for helping in the nanocoating fabrication.

I am so thankful to Dr. Yaw Adu-Gyamfi for serving as a committee member. I also want to thank Dr. Sarah Orton, Dr. Bret Ulery, and Dr. Maria Fidalgo for their help by allowing me to access their labs and equipment to complete this research. Special thanks to the electron microscopy center (EMC) staff, Dr. Tommi White and Dr. Davide Stalla, for their partial funding for this project and helping in the SEM characterization. Thanks to Mr. Ghassan Al Bahhash, Mr. Michael Carraher, Mr. Mike Harlow, and Mr. Ron Monson for their help in completing many experiments of this thesis.

I am thankful to my lovely family for their patience and support, starting with my great husband Ahmed who without him I will never complete my degree. To my lovely kids Mohammed, Rahma, Sarah and finally my sweaty Ibrahim (BoBo). I am sorry for missing a lot of important and lovely moments in your lives. My heart goes to my parents, especially my mom, who her heart, support, and prayers are always with me.

Table of Contents

DEDICATION ..... **ii**
ACKNOWLEDGEMENTS ..... **iii**
LIST OF ILLUSTRATIONS ..... **vi**
LIST of ABBREVIATION ..... **ix**
ABSTRACT ..... **xi**
Chapter One: Introduction **1**
1.1 General 1
1.2 Literature review 6
1.3 Research objective 14
1.4 Thesis structure 16
Chapter Two: Materials and Methods **17**
2.1 General 17
2.2 Materials 17
2.3 Synthesis of Al_2O_3 coating on CNFs 19
2.4 Improper Al_2O_3/CNFs dispersion technique 19
2.5 Dispersion of bare CNFs and Al_2O_3/CNFs and fabrication of mortars 20
2.6 Characterizations 24
2.6.1 Transmission electron microscopy (TEM) 24
2.6.2 Scanning electron microscopy (SEM) 25
2.6.3 Energy dispersive X-ray spectroscopy (EDS) 26
2.7 Thermogravimetric analysis (TGA) 27
2.8 X-ray powder diffraction (XRD) 29
2.9 BET and pore volume measurements 30
2.10 Mechanical characterizations 30
2.11 Workability (fluidity) 31
2.12 Freeze-thaw testing 32
2.13 Drying shrinkage 35
Chapter Three: Results and Discussion **38**
3.1 General 38
3.2 Dispersion of bare CNFs and Al_2O_3/CNFs 38
3.3 Characterizations results 39

3.3.1. Transmission electron microscopy (TEM) 40
3.3.2 Microstructure analysis 41
3.4 Compressive strength of composites 47
3.5 Workability (fluidity) 52
3.6 Cement hydration by thermal analysis (TGA) 53
3.7 X-ray diffraction (XRD) 57
3.8 Freeze-thaw effects 60
3.8.1 Mass loss 60
3.8.2 Compressive strength post freezing-thawing cycles 62
3.8.3 Physical appearance 64
3.9 Pore structure results 67
3.10 Drying shrinkage results 68
Chapter Four: Conclusion and Recommendations 72
4.1 General 72
4.2 Conclusions 72
4.3 Recommendations 75
BIBLIOGRAPHY 77
Appendix 85

LIST OF ILLUSTRATIONS

List of Figures

Figure 1.1 Ultimate point of compressive strength response . 2
Figure 1.2 Cement microstructure pore size distribution . 3
Figure 1.3 Representation of the water movement at different relative humidity . 5
Figure 1.4 Disjoining pressure, (a) Dry cement, (b) Adhered water with cement [adapted from [16]]. 6
Figure 1.5 Carbon nanomaterials (a) CNTs single and multiwall, (b) CNFs, (c) Graphene oxide sheets 8
Figure 1.6 TEM images of Ni-CNTs of Ni nanoparticles at different aspect ratio. 14
Figure 2.1 (a) CNFs in powder form, (b) TEM image at 200 nm scale, (c) Al_2O_3/CNFs in powder form, and (d) TEM image at 200 nm scale. 18
Figure 2.2 Al_2O_3/CNFs aqueous solutions showing excessive amount of air bubbles during mixing with superplasticizer. 20
Figure 2.3 Sonication setup showing; (1) Sonicator, (2) Probe diameter size of 10 mm, (3) Al_2O_3/CNFs, or CNFs with superplasticizer suspension, and (4) Hot plate stirrer. 21
Figure 2.4 Al_2O_3/CNFs or CNFs suspension pouring during mixing with cement and sand. 22
Figure 2.5 A cartoon displays the steps of cement mortars preparation when the Al_2O_3/CNFs used. 23
Figure 2.6 JEOL JEM 1400 located in the electron microscopy core facility at the University of Missouri. 24
Figure 2.7 FEI Quanta 600 FEG SEM scope located in electron microscopy core facility at the University of Missouri. 26
Figure 2.8 Preparation the samples for EDS analysis inside a washer disc. 27
Figure 2.9 Sample preparation for TGA (a) Grinding the cement, (b) Alumina pan holds 23 mg of the powder, (c) TGA (Q-500) 28
Figure 2.10 Compressive strength test apparatus (Forney machine). 31
Figure 2.11 Flow table apparatus 32
Figure 2.12 (a) Freeze-Thaw cycling test apparatus. (b) Samples under freezing conditions. 34
Figure 2.13 Freeze-thaw chamber temperature set range of 18°C to 4°C (0°F to 40°F) 35
Figure 2.14 (a) Length comparator and dial gauge, (b) Steel prism molds of dimensions 1"×1"×10", 2-Gang. (c) Cement mortar prisms samples in controlled-humidity room. 37
Figure 3.1 CNFs and Al_2O_3/CNFs dispersion in water after one month. 39
Figure 3.2 Bright field transmission electron microscopy (TEM), (a) TEM image shows the uncoated CNFs, (b) TEM image shows the Al_2O_3 coating on CNFs, the inset shows high magnification TEM image shows the layer morphology, (c) BET analysis for Al_2O_3/CNFs with its 40
Figure 3.3 SEM images at different magnifications at 5000x and 10000x: (a and b) CNFs embedded cement mortar, (c and d) Al_2O_3/CNFs embedded cement mortar, all at the age of 28 days. 42
Figure 3.4 Micro cracks in (a) Control sample (C0) at magnification of 5000x, (b) Al_2O_3/CNFs-mortar composites at magnification of 10000x. 43
Figure 3.5 EDS spectrum and elements mass percent for C0. 44

Figure 3.6 Elementals mapping from X-ray for a selective area of the cement mortar of Al_2O3/CNFs-0.125% (a) C, (b) Al, (c) Ca, (d) Si. 45
Figure 3.7 EDS spectrum and elements mass percent for Al_2O_3/CNFs-0.125% 45
Figure 3.8 Elementals mapping from X-ray for a selective area of the cement mortar of CNFs-0.25% (a) C, (b) Al, (c) Ca, (d) Si. 46
Figure 3.9 EDS spectrum and elements mass percent for CNFs-0.25%. 47
Figure 3.10 Compressive strengths at age of 7, 14, and 28 days for various specimens. 48
Figure 3.11 Filler effect of the CNFs inside the cement mortar matrix. 49
Figure 3.12 SEM images of Al_2O_3/CNFs in mortar composites 50
Figure 3.13 TGA analysis for C0, CNFs-0.25%, and Al_2O_3/CNFs-0.125, (a) 7 days, (b) 14 days, (c) 28 days. 56
Figure 3.14 TG/DTA analysis of weight losses of C0, CNFs-0.25 % and Al_2O_3/CNFs-0.125 % mortars. 57
Figure 3.15 XRD patterns total spectrum (a) C0, (b) CNFs-0.25, (c) Al_2O_3/CNFs-0.125%. 59
Figure 3.16 Selective peaks (a) C_3S and C_2C peak and (b) CH peak for C0, CNFs-0.25, and Al_2O_3/CNFs-0.125%. 59
Figure 3.17 Mass loss ratios of mortars samples exposed to freezing-thawing cycles. 61
Figure 3.18 Compressive strength for C0, CNFs-0.125% and Al_2O_3 /CNFs-0.125% composites after exposing to freezing-thawing cycles. 63
Figure 3.19 Samples after 50 freeze-thaw cycles, (1) C0, (2) CNFs-0.125%, (3) CNFs-0.25%, (4) Al_2O_3/CNFs-0.125%, (5) Al_2O_3/CNFs-0.25%, (6) Al_2O_3/CNFs-0.5%. 65
Figure 3.20 Samples after 150 freeze-thaw cycles, (1) C0, (2) CNFs-0.125%, (3) CNFs-0.25%, (4) Al_2O_3/CNFs-0.125%, (5) Al_2O_3/CNFs-0.25%, (6) Al_2O_3/CNFs-0.5%. 65
Figure 3.21 Samples after 300 freeze-thaw cycles, (1) C0, (2) CNFs-0.125%, (3) CNFs-0.25%, (4) Al_2O_3/CNFs-0.125%, (5) Al_2O_3/CNFs-0.25%, (6) Al_2O_3/CNFs-0.5%. 66
Figure 3.22 (a) BET isotherm analysis, (b) Pore volume distribution. 68
Figure 3.23 (a) Drying shrinkage of the CNFs composites at different ratios in comparison with control sample at different ages. (b) Drying shrinkage of the Al_2O_3/CNFs composites at different ratios with comparison to control sample at different ages. 69

List of Tables

Table 2.1 Chemical and physical properties of the cement 18
Table 2.2 Properties of CNFs 18
Table 2.3 Mixing proportions recipes and nanomaterials contents 23
Table 3.1 Compressive strength at different curing ages of 7, 14 and 28 days. 51
Table 3.2 The slump tests data 53
Table 3.3 TGA/DTA analysis of mass losses for specimens C0, CNFs-0.25%, and Al_2O_3/CNFs-0.125%. 54
Table 3.4 Summary of rapid freezing and thawing results 62
Table 3.5 Compressive strength for C0, CNFs-0.25, and Al_2O_3/CNFs 0.125 hardening samples after exposing to freeze-thaw cycles. 64
Table 3.6 Average drying shrinkage results for C0, CNFs-composites, and Al_2O_3/CNFs-composites at different curing ages 70

LIST of ABBREVIATION

Aft: Ettringite

ASTM: American Society for Testing and Materials

ALD: Atomic Layer Deposition

Al_2O_3: Aluminum oxide

BET: Brunauer-Emmett-Teller

BJH: Barrett-Joyner-Halenda

BSE: Backscattered Electron

$CaCO_3$: Calcium carbonate

C-A-H: Calcium-aluminate-hydrate

CF: Carbon fiber

CH: Calcium hydroxide

CLD: Condensed Layer Deposition

CNFs: Carbon nanofibers

CNTs: Carbon nanotubes

C-O-C: Epoxy groups

COOH: Carboxyl groups

C-S-H: Calcium-silicate-hydrate

C_2S: Dicalcium silicate

C_3S: Tricalcium silicate

CuO: Copper oxide

CVD: Chemical Vapor Deposition

DOH: Degree of hydration

DTA: Derivative thermal analysis

EDS: Energy Dispersive X-ray Spectroscopy

GO: Graphene oxide

MNPs: Metal oxide nanoparticles

MOPs: Metal oxide nanomaterials

Ni: Nickel oxide

OH: Hydroxyl groups

RH: Relative humidity

SE: Secondary Electron

SEM: Scanning Electron Microscopy

SiO_2: Silica dioxide

SP: Superplasticizer

TEM: Transmission Electron Microscopy

TGA: Thermogravimetric Analysis

TiO_2: Titanium dioxide

UHPC: Ultrahigh performance concrete

XRD: X-ray powder diffraction

ZrO_2: Zirconium dioxide

ENHANCING THE MECHANICAL AND DURABILITY PROPERTIES OF CEMENT MORTARS BY USING ALUMINA NANOCOATING ON CARBON NANOFIBERS

Huda Alqader

Dr. Hani Salim, Thesis Supervisor

ABSTRACT

This thesis presents a comparative study on using nanocomposite of aluminum oxide (Al_2O_3) nanocoating on carbon nanofibers (CNFs) and bare CNFs for enhancing the cement mortars mechanical properties, durability under freeze-thaw conditions, and mitigating the drying shrinkage. Although CNFs work to bridge the cracks in cement and to improve the strength, their pristine surface is relatively inert. On the other hand, metals oxides nanomaterials have shown a remarkable surface reactivity, nevertheless, they offer less bridging role. Herein, we close the gap by combining the two parameters, the bridging, and the surface reactivity. This is done by fabricating porous Al_2O_3 nanocoating on carbon nanofibers denoted as, Al_2O_3/CNFs. The Al_2O_3 layer offers a certain degree of pozzolanas in a form of a nanofilm that possesses a high specific surface area of 274.3 m^2/g. Several characterizations such as Transmission Electron Microscopy (TEM), Scanning electron microscopy (SEM), and Energy Dispersive X-ray Spectroscopy (EDS) have been conducted to study the coating, mortar's microstructure, and elements mapping. Brunauer-Emmett-Teller and Barrett-Joyner-Halenda (BET-BJH) analysis was employed to detect the porosity, whereas Derivative thermal analysis- differential thermogravimetric (TGA-DTG) and X-ray powder diffraction (XRD) have been coupled to investigate the hydration mechanism. The Al_2O_3/CNFs samples with mass ratios of 0.125%, 0.25%, 0.5% of the

cement were compared with bare CNFs with the same mass ratios of 0.125%, 0.25%, 0.5%, and with a plain sample as a reference. The compressive strength before and after freeze-thaw cycles of the Al_2O_3/CNFs-0.125% and CNFs-0.25% have shown the highest performance relative to the reference sample. The mass loss due to the freeze/thaw conditions was significantly reduced by addition of Al_2O_3/CNFs at different ratios comparing to composites that contain CNFs with different ratios and comparing to reference samples. The better performance was shown with the most reduction obtained for the Al_2O_3/CNFs-0.125%, Al_2O_3/CNFs-0.5% and CNFs-0.25%, respectively. In addition, the Al_2O_3/CNFs-0.125% and CNFs-0.25% have shown the least drying shrinkage. The results of this study demonstrated that the Al_2O_3 nanofilm along with CNFs improved the microstructure bridging, enhanced the hydration gel production, and refined the microstructure pores. All these favorable properties improved the overall mechanical properties, freeze-thaw durability, and drying shrinkage.

Chapter One: Introduction

1.1 General

Nowadays, cementitious composites are the most prevalent construction materials. However, they suffer from a low tensile strength and are highly susceptible to cracking. As a result, many attempts have been dedicated in enhancing the cement structure either by macro-level or micro-level reinforcements [1, 2]. Researchers have studied various phenomena the cementitious composites experience such as mechanical failure, shrinkage, and durability. Durability against freeze-thaw deterioration is one of the most significant needs in areas subjected to extreme cold durations and temperature fluctuations. Over time, when exposed water in cementitious composites freezes and thaws repeatedly, a series of internal micro-cracks will be created. On the other hand, for shrinkage, there are three types of shrinkage, plastic, autogenous, and drying shrinkage have been studied. Drying shrinkage, the focus of this thesis, takes place when a cementitious composite is exposed to the environmental conditions resulting in a volume change, and it is the most widely recognized source of volume change in cementitious composites.

It is generally accepted that the internal voids or cracks in the cementitious materials start from a nano size as embryo then they propagate to micro scale cracks and up to destructive cracks. If the voids population is largely present in the first place, mechanical failure, severe drying shrinkage, and weak durability are often expected. The compressive strength is a stress under which a solid material sustain load without fracture. Brittle materials experience fracture as they reach their ultimate compressive strength (Figure 1.1), while ductile materials deform, and a certain level of the deformation can be considered as a

strength limit. The compressive strength of cementitious materials is influenced by many factors such as structure density, degree of hydration, and water-cement ratio. The microstructure of the cementitious material has a direct influence on the compressive strength. When the internal structure is dense, the material response to the applied force will be sufficient to maximize the ultimate point value.

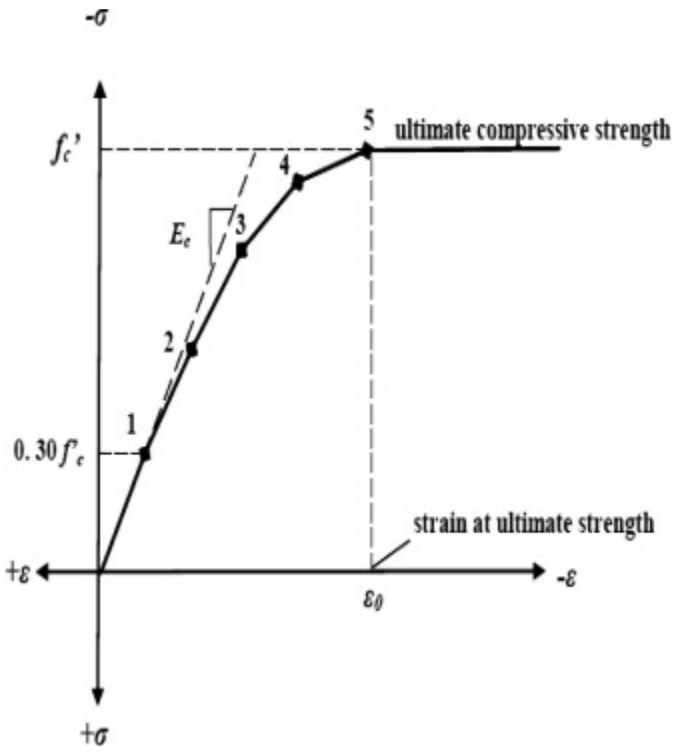

Figure 1.1 Ultimate point of compressive strength response [3].

Another property of interest to this research is durability represented by frost resistance. When a cementitious material is repetitively exposed to freezing and thawing cycles, the micro-structure may severely deteriorate. Freeze-thaw effects are explained by critical saturation theory, the hydraulic pressure theory, and osmotic pressure theory [4]. In critical saturation theory, the cementitious materials experience damage when at least 91% of the capillary pores are filled by water [5]. This is associated with the ice volume expansion by at least 9% causing a further expansion in the voids [6, 7]. This expansion induces a capillary pressure that manifests an internal

stress which causes internal cracking if it exceeds the material local strength limit. The hydraulic pressure is initiated by the pressure build up due to the resistance of unfrozen water in cement capillaries. If the cement does not expand when the water freezes, the unfrozen water will be expelled far from the freezing regions leading to a structure damage [8]. The osmotic pressure theory states that the water transfers from gel pores to the capillary via the diffusion phenomenon [9]. This is thermodynamically reasonable as the gel pores has a higher energy than the capillary pores due to the size difference. The water in small gels pores does not freeze at the same temperature of the larger capillary pores. Since the unfrozen water has a higher free energy than the ice, then it continues to flow until the equilibrium takes place. Figure 1.2 shows relative pore sizes and distribution of cementitious composites.

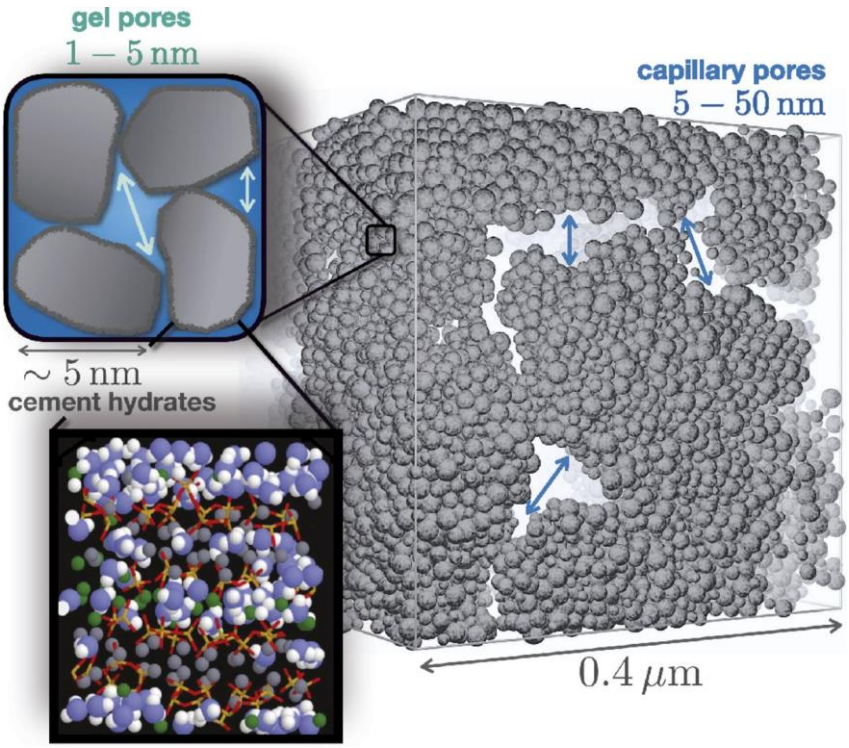

Figure 1.2 Cement microstructure pore size distribution [10].

Drying shrinkage is a phenomenon in which the volume of the cement hydrated products experiences a change, mostly reduction. There are many factors affecting the shrinkage rate such as the properties of the components, proportions of the components, degree of

humidity during curing process, and drying conditions [11]. If the relative humidity is 100%, the number of water molecule leaving the liquid phase equals to the number of molecules entering back. Therefore, no evaporation is expected to take place. When the relative humidity drops less than 100%, the drying begins as the water vapor pressure on the water surface will not equal the saturation pressure.

Four theories related to the drying shrinkage will be briefly reviewed here. Capillary tension theory occurs when water evaporates until a meniscus is formed with a radius of curvature corresponding to a known relative humidity as described in Kelvin-Laplace equation [12]. A further decrease in the relative humidity leads to increasing in the meniscus radius until it equals to the pore radius. When they are equal, the meniscus radius is defined as "minimum radius". If the relative humidity drops less than the relative humidity that corresponds to minimum radius, the water will be totally evaporated. In a cementitious paste, the pores sizes are not uniform. Therefore, in the time the big pores be emptied, the meniscus is formed in the pores that have an equal radius with meniscus. This puts the water in the capillary under tensile stress which later to be balanced by a compressive strength by the solid structure which results in a reduction in the volume (shrinkage). It is worthwhile to mention, this theory is valid with a humidity range of 40-100 % [13, 14].

The second theory is the surface tension. The water molecules on the surface lack equilibrium, and therefore they need a compensation force equals by value, defined as "surface tension". Since the cementitious paste has a high surface area, there is a huge compressive stress in the order of 250 MPa [15, 16]. If there is a change in the stress levels,

a change in the volume will take place causing the shrinkage. Some researchers have suggested that this mechanism is valid only for surface-adsorbed water at a relative humidity of 40%. Others have proposed that this mechanism could be applied at 5% 50% relative humidity [15].

Another mechanism has been proposed in explaining the drying shrinkage is the movement of interlayer water [17]. The hydration products such as calcium-silicate-hydrate (C-S-H) are comprised of layers forming the microstructure. When the water enters among these layers, they are separated. The moving of the water in and out the C-S-H layers creates a space disturbing which results in a length change. Most researchers classified this mechanism at a relative humidity below 35–40%, see Figure 1.3.

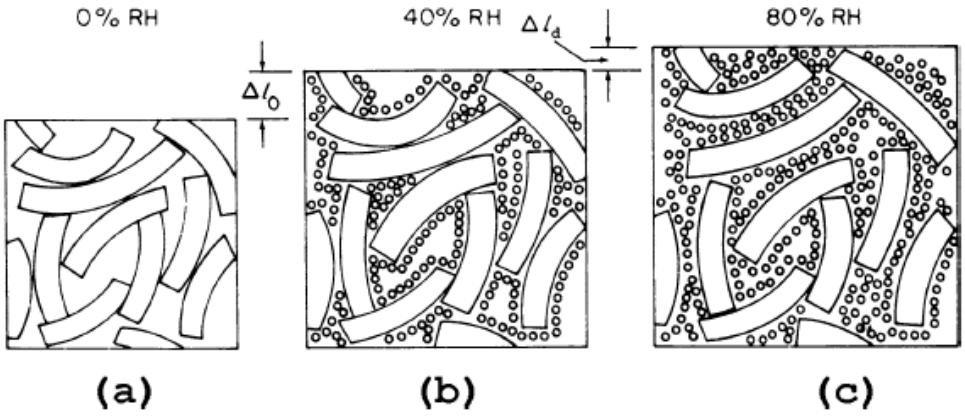

Figure 1.3 Representation of the water movement at different relative humidity [17].

Lastly, disjoining pressure theory has also been discussed [13]. The disjoining pressure evolves when the water molecules repel each other among the C-S-H particles. This produces a decrease in the bonding forces which are represented by Vander Waals [Ref] among the C-S-H microstructure. The repulsion force and less bonding lead to a change in the volume as shown in Figure 1.4. That said, the disjoining pressure mechanism was under a noticeable debate. Power [13] has suggested that this mechanism is valid over a whole

range of humidity. While Munich [14] said to be applied only beyond a relative humidity of 50%, the mechanism was totally denied by Feldman and Sereda.

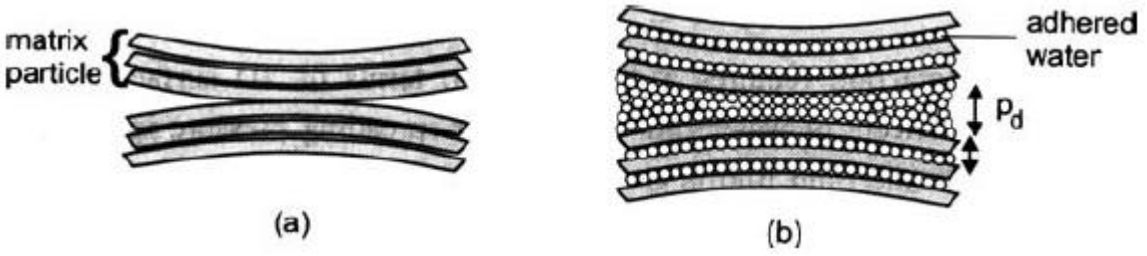

Figure 1.4 Disjoining pressure, (a) Dry cement, (b) Adhered water with cement [adapted from [16]].

In tackling the aforementioned drying shrinkage problems, researchers have sought to find substantiable solutions. Such solutions are modifying the mixing recipes and embedding either macro, or micro fillers, and even nanomaterials. In the next literature review section, previous works on using nanomaterials that are claimed as solutions are reviewed.

1.2 Literature review

In this section, previously published works that have reported efforts on tackling the mechanical properties (compressive strength), the durability (frost resistance), and drying shrinkage using nanotechnology are broadly presented. It has been widely accepted that compacting cementitious materials increases the cementitious material performance in all those parameters. Therefore, reinforcement is intentionally used to prevent voids initiating at the first place as an effective way to protect and to enhance the performance of the cementitious materials properties [18-20]. Researchers have found that nanomaterials are highly effective with cementitious materials as they can act as seeding sites for the hydration products [21]. The hydration reaction is catalyzed by either oxygen functional groups (i.e., - OH, - COOH,- C=O) on carbon nanomaterials or via the pozzolanic reactivity

associated with some metals oxides nanoparticles (i.e., SiO_2, Al_2O_3) [22].This mainly serves in porosity refinement, water impermeability, and structure bridging. In the next three subsections, three types of nanomaterials that are used in tackling the three issues will be demonstrated.

1.2.1 Carbon nanomaterials

Carbon nanomaterials such as carbon nanotubes (CNTs), carbon nanofibers (CNFs), graphene, graphene nanoplates and graphene oxide, possess superior physical, chemical and mechanical properties. These nanomaterials have been successfully embedded into cementitious materials to enhance the mechanical properties, durability, and electrical/ thermal conductivity [23, 24]. Many researchers have studied CNTs usage in various applications such as energy storage, biomedical materials, electronic and beyond [25, 26].

CNTs are made from graphene sheets with nanometer dimensions and a hollow structure. Based on the number of rolled layers of graphene, CNTs can be classified into single-walled CNTs and multi-walled CNTs as shown in Figure 1.5 (a). CNTs are known as the strongest and stiffest materials yet discovered in term of tensile strength and elastic modulus. The Young's modulus and tensile strength could reach up to 1 TPa and 100 GPa, respectively, for individual one-dimensional CNT [27]. CNTs are stronger than steel by 100 times. CNFs are another carbon nanomaterial that could offer a similar benefit of using CNTs. On the other hand, CNFs shown in Figure 1.5 (b) have a unique dimension as they have a combined microscopic length from 50 to 100 μm with a nanoscale diameter between 50-200 nm. Compared to CNTs, CNFs have a lower production cost by being 3 to 10 times cheaper than CNTs production cost [28].

Since its discovery in 2004 [29], many researchers have used graphene in cementitious materials and was experimentally and theoretically studied. This two-dimensional crystal is a single layer of carbon atoms arranged in a hexagonal lattice. One of its unique properties is the high surface area of 2,630 m^2/g and Young's modulus of 1 TPa. When the graphene oxidized, it is called graphene oxide (GO) which is one of the important derivatives of graphene. GO, shown in Figure 1.5 (c) is rich in oxygen-containing functional groups such as hydroxyl (-OH), epoxy (-C-O-C), and carboxyl (-COOH) on the edges.

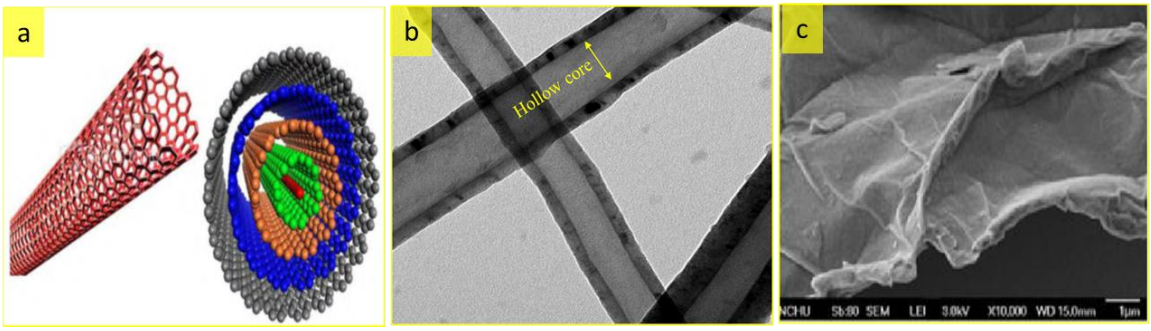

Figure 1.5 Carbon nanomaterials (a) CNTs single and multiwall [30], (b) CNFs, (c) Graphene oxide sheets [31]

1.2.2 Effect of carbon nanomaterials in cementitious materials

In the recent decade, there has been a growing interest in integrating carbon nanomaterials in cement composites to increase the frost resistance, mechanical strength, and drying shrinkage [23, 32-34] [35] [24]. In term of enhancing the frost resistance, the efforts have focused on either eliminating the voids formation or refining them to small sizes to reduce the permeability of the cementitious material, hence improving the strength and durability. Some researchers have reported allowing extra space for ice to expand by incorporating air bubbles in the composites [22]. Limited studies have explicitly reported using CNFs in

enhancing the cement frost resistance. Cwirzen et al. [35] studied the effect of the CNFs on the strength and residual cumulative strain of cement mortars after freeze-thaw cycles with a high water-cement ratio of 0.5. They found the higher content of the CNFs composites shows a lower ultimate strain and less internal damage. Their study also indicated the bridging ability of CNFs with higher water ratio. Wang et al. [36] has comparatively investigated the different CNFs loading effect on frost resistance. They found 0.3% of CNFs dosage to be an optimum choice that refines the microstructures which promoted the durability. Metaxa et al. [37] showed the ability of the CNFs against the crack growth in the cement matrix. In their results, the CNFs have well-performed in reducing the crack propagation by a bridging phenomenon and providing a load transfer across cracks and pores. However, the CNFs performance is controlled by the well dispersion of CNFs [38].

The inadequate interfacial interaction between CNFs nanomaterials and cementitious composites is another factor that influences the nanoscale reinforcement. This is mainly due to the smooth surface of the CNFs that can have a weak bond with cement matrix. Therefore, surface treatment is essential to improve the solubility as well as the bonding with cement hydration products. One type of this treatment is using covalent methods by providing a functional group on the surface of CNFs [39]. The existence of CNFs in composites does not participate in formation any additional hydration products. Based on the literature, the outstanding performance of using the CNFs is due to the bridging, refining and nucleating effects [40]. Improving the dispersion of the CNFs and increasing the bonding strength at a nanoscale by adding an effective layer remain as hurdles.

Carbon nanomaterials have also appreciable role in mitigating the drying shrinkage. Wang et al. [41] have investigated the effect of CNFs on drying shrinkage in ultrahigh performance concrete (UHPC). They found the CNFs can further refine the capillary pores resulting a reduction in the drying shrinkage due to the nanoscale size of the CNFs. On the same trend, Fu et al. [42] have found using the ozone-treated carbon fibers (CF) significantly reduced the drying shrinkage in cement samples. This was attributed to the highly hydrophilic surface with a water contact angle of zero. In using CNTs, long-time drying shrinkage concrete has been improved by 5% and 18% as compared to the reference concrete, while the early age dry shrinkage improved by 54% as reported by Hawreen et al.[43]. Lee et al. [44] have demonstrated using nano-clay and graphite nanofiber to be effective in reducing the early age shrinkage by nearly 70%.

1.2.3 Metal oxides nanomaterials

Metal oxide nanomaterials are considered as important technological materials in numerous applications. Due to their unique properties, metals oxides nanomaterials manufacturing is continuously under modifications and improvements. The unique properties such as a high ductility and a high density relative to volume enable them to be vastly used in the modern technology. In their fabrication methods, wet chemistry such as hydrothermal, sol-gel and dry chemistry such as chemical vapor deposition (CVD) and atomic layer deposition (ALD) are usually used. Such metals oxides are CuO, TiO_2, ZrO_2, Al_2O_3, and SiO_2. They have been integrated in all modern technologies such as nano-membranes, nano-chips, nano-catalysis, nano-batteries, building structure materials and beyond [45].

Metal oxides nanomaterials have been extensively used for the enhancement of the cementitious materials. Such metal oxides are TiO_2, ZrO_2, SiO_2, and Al_2O_3. Each one of the oxides behave differently inside the cement composites based on their geometry (1-D, 2-D, or 3-D), their surface chemistry (hydrophilic or hydrophobic), and their intrinsic reactivity with cement (pozzolanic performance). Regarding the geometry, 1-D and 3-D such as (nanotubes and nanoparticles) are the widest used due to the low manufacturing cost comparing with 2-D [46]. The hydrophilicity surface nature is generally needed to participate in the hydration reaction. Some metal oxides such as SiO_2 and Al_2O_3 have an intrinsic property called "pozzolanic reactivity". This activity is defined as they react with calcium hydroxide at the presence of water to produce secondary cementitious gels that enhance the cement performance.

1.2.4 Effect of metal oxides in cementitious materials

Metal oxides nanomaterials (MONs) have been vastly considered in reducing the porosity of the cement composites. These materials possess a high surface area that makes them reactive to strengthen the microstructure of the cement with less porosity [47, 48]. Especially, those that possess a pozzolanic property such as silica and alumina nanoparticles [49-51]. Those materials react with calcium hydroxide $Ca(OH)_2$, portlandite, forming a secondary reaction producing gels of calcium-silicate-hydrate (C-S-H), calcium-aluminum-hydrate (C-A-H). The reaction of nano alumina with calcium hydroxide that produced from the hydration of calcium aluminates. Rate of such a reaction is controlled by the available surface area and the surface nucleation sites [52]. Behfarnia [49] has reported the feasibility of using both SiO_2 and Al_2O_3 nanoparticles in enhancing the frost resistance of the concrete mixtures due to the pozzolanic and refining effects.

However, an inhomogeneous dispersion for these nanoparticles could level down their job such as forming aggregates inducing big sizes voids formation. Unlike CNFs or CNTs, MONs (nanoparticles) lacks the bridging phenomenon which is needed in compacting the cement microstructure unless they are manufactured as metal oxides nanotubes.

Another issue is the cost for using the MNPs at a large scale when the idea is about to scale up. A smart design for metal oxides nanoparticles such as a high surface area, hydrophilic surface, and a low cost are needed for the feasibility. Metal oxides have appreciable published data in the literature on drying shrinkage. In their study, Zhang et al. [53] have shown the effect of TiO_2 on the drying shrinkage. They found TiO_2 indeed mitigates the drying shrinkage due to refining the pore structure. Wang et al. [54] have investigated the effect of nano-SiO_2 on volume shrinkage. Surprisingly, they reported the nano-SiO_2 induces the volume shrinkage relative to the plain sample due to a fast hydration reaction. On the other hand, Abdel-Gawwad et al.[55] have studied the effect of magnesia and alumina nanoparticles on drying shrinkage. Their outcomes show a significant reduction in the shrinkage which was assigned to the formation of the secondary moieties of C-S-H and C-A-H.

1.2.5 Effect of binary nanomaterials in cementitious materials

Combining carbon nanomaterials and metal oxides is a promising approach in improving the interfacial interaction of the carbon materials with cement, enhance the dispersion, and retaining the bridging resulting in enhancing the mechanical properties and the durability of cement [56-61]. Such combinations are nanoparticles incorporation or metal oxides nanocoating. Zhang et al. [62] have reported dual fillers of TiO_2 and CNTs in cement aiming to make a multifunctional cement. They reported a significant increase in the

dispersion of CNTs when the TiO_2 is present. In line with that, Gurumurthy et al. [63] have shown similar results of increasing the dispersion when Al_2O_3 nanoparticles are used with CNTs. Moreover, they found a remarkable increase in the compressive strength relative to the plain specimen.

A more recent study has shown a significant improvement in carbon nanotubes dispersion and good bonding with the cementitious material after silica nanoparticles incorporation [60]. Sikora et al. [59] have reported a comparison between CNTs and SiO_2-CNTs on cement compressive strength under elevated temperatures. They found that adding silica in a form of nanocoating with a dense layer has remarkable effect on increasing the bond and even protect the CNTs from being oxidized at a high temperature. The hybrid nanocomposite has a crucial role in drying shrinkage mitigation. Tafesse et al. [64] have partially studied the role of using the CNTs /fume silica in the drying shrinkage. They reported no or negligible effect of embedding the CNTs especially at a low water/cement ratio. However, Song et al. [65] have shown using silica fume with CNTs have remarkably reduced the drying shrinkage due to the dispersion improvement. Dong et al. [66] have reported a study on coating the CNTs by nickel nanoparticles and their role in the cement as shown in Figure 1.6. They studied different aspect ratios and volume loading in the cement microstructure. They found coupling Ni/CNTs has increased the dispersion and the compressive strength.

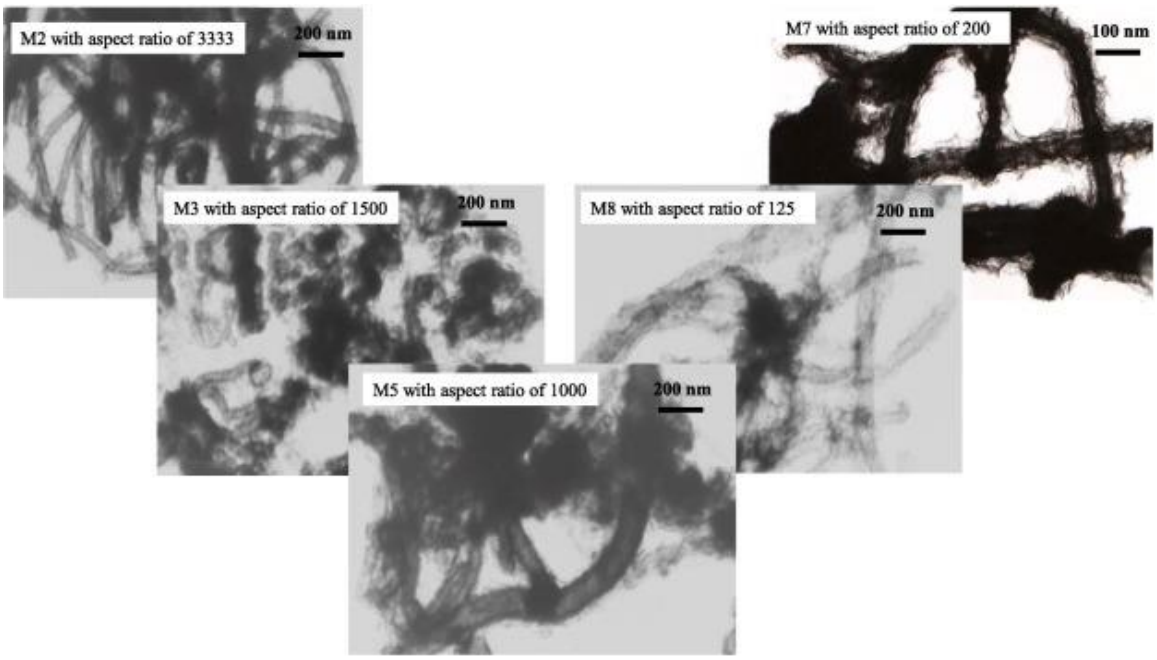

Figure 1.6 TEM images of Ni-CNTs of Ni nanoparticles at different aspect ratio.

1.3 Research objective

Durability issues in the cementitious materials are often due to weather changes, such as cold, hot, and dry weather. Due to their porous structure and brittleness, cementitious materials are highly vulnerable to freeze-thaw cycles and drying shrinkage, which lead to lowering their strength. In addition to durability, sustainability issues require ongoing maintenance to prolong the service life of cementitious composites. Maintenance cost usually represents a high portion of initial construction cost. Therefore, improving durability and strength of the cementitious composites became a necessity. Nanomaterials have unique physical, mechanical, and chemical properties due to their nano size. Carbon nanomaterials have shown an effective nano scale reinforcement due to their bridging, filling, and a certain degree of nucleation effects. On the other hand, metals oxides nanomaterials have proven to play an effective role in reinforcing cementitious composites.

The metals oxides performance is governed by filling the porous, rich nucleation sites that promote the hydration process. Some types of metals oxides can even participate in hydration process by providing pozzolanic effect leading to producing additional hydrated gel. Based on the literature, combining the two nanomaterials can be an effective tool to have a nanocomposite that possesses both nanomaterials' properties. The binary nanomaterials could overcome some limitations such as the nanomaterial dispersion and strong bonding with the cement matrix.

Therefore, this thesis will focus on evaluating the performance enhancement of the embedment of carbon nanofibers coated with aluminum oxides into cementitious composites. A core-shell structure of carbon nanofibers as a core and porous-fluffy alumina as a shell denoted Al_2O_3/CNFs at a loading percentage of 42 wt.% and 58 wt.% of Al_2O_3 and CNFs, respectively, is investigated. The advantages of using such materials are low cost, high specific surface area, high dispersion with pozzolanic property, and retaining the bridging property. This study investigates the compressive strength, frost resistance, and drying shrinkage of the cement mortar. Three ratios of 0.125%, 0.25%, and 0.5% of the Al_2O_3/CNFs and bare CNFs were compared with each other and with a control sample set. Results have shown the 0.125% of Al_2O_3/CNFs and 0.250% of CNFs performed the best in all experiments.

The work has two main parts. The first one is the preparation of the nanomaterial either for the nanocoating or for using directly. This is done by surface functionalization using a solution mixture of sulfuric acid and nitric acid. Afterwards, the Al_2O_3 nanocoating was conducted following the process described in reference [67]. The second part is embedding the prepared nanomaterials inside the cements mortars composites. Various

characterizations were utilized to examine coated nanomaterials and the reinforced cement mortar composites, such as TEM, SEM-EDS, TGA, XRD, and BET-BJH, which are described in this thesis.

1.4 Thesis structure

This thesis is composed of four chapters. Chapter one introduces the general background of the topic with problem description and the research objectives. Chapter one also introduces literature review including the most relevant and up-to-date studies related to using nanotechnology in reinforcing cementitious composites, definitions and properties of carbon nanomaterials, metals oxides nanomaterials, and hybrid nanomaterials. Chapter two describes the materials and the synthesis processes of the hybrid nanomaterials Al_2O_3/CNFs, mixture designs, and methodologies of different characterizations.

Chapter three presents the results and discussion of different types of characterizations, including the influence of the nanomaterials on the workability, hydration process, microstructure characteristics, and mechanicals and durability properties. Finally, Chapter four presents the conclusions and provides recommendations with proposed future research.

Chapter Two: Materials and Methods

2.1 General

This chapter presents the materials that were used in the study including the cement, sand, and other chemicals. Furthermore, the synthesis processes starting from the nanocoating of Al_2O_3 on CNFs to cement mortars fabrication. The specimens' characterizations were also included such as scanning electron microscopy (SEM), thermal analysis (TGA), X-ray diffraction (XRD), Brunauer–Emmett–Teller (BET), and. Barrett-Joyner-Halenda (BJH). Lastly, the performance tests were also reported such as compressive strength, workability, Freeze-Thaw, and drying shrinkage.

2.2 Materials

Ordinary Portland cement classified within the ASTM C150 standard type I was utilized to make the mortar mix. Chemical composition and physical properties of the cement are depicted in Table 2.1. Natural river sand with a fineness modulus of 2.6 was used in all mixes. To enhance the workability, A water-reducing admixture (Master Glenium-7500 from BASF) was used in the mixtures. However, in the case of the mixtures that contain CNFs dosages, a superplasticizer (SP) was used as a surfactant to help in dispersion of these material in water. Carbon nanofibers were provided from Pyrograf Products. The properties of CNFs are shown in Table 2.2. For the coating purpose, trimethylaluminum (TMA-1.0M) as a precursor was obtained from Sigma-Aldrich. The transmission electron microscopy images of the CNFs and Al_2O_3/CNFs are shown in the Figure 2.1 (a-d).

Table 2.1 Chemical and physical properties of the cement

SiO_2	Al_2O_3	Fe_2O_3	MgO	CaO	SO_3	C_3A	Specific surface area (cm^2/gr)	Compressive strength, 7- day (kg/cm^2)	Compressive strength, 28-day (kg/cm^2)
22%	5%	3.82%	1.9%	64%	1.5%	6.5%	3000	275	370

Table 2.2 Properties of CNFs

Diameter (nm)	Length (μm)	Surface area (m^2/g)	Dispersive energy (mJ/m^2)	Elastic modulus (GPa)	Strength (GPa)	Electrical resistivity (μΩm)	Aspect ratio
50-150	5-20	41	135	600	6.7	-	100 -1000

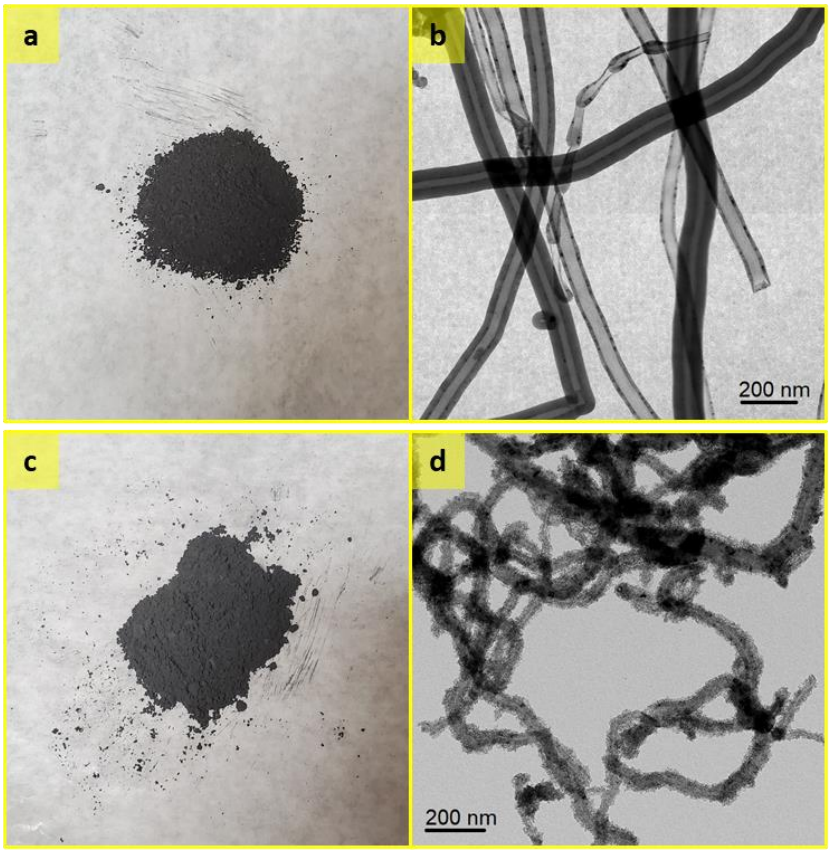

Figure 2.1 (a) CNFs in powder form, (b) TEM image at 200 nm scale, (c) Al_2O_3/CNFs in powder form, and (d) TEM image at 200 nm scale.

2.3 Synthesis of Al_2O_3 coating on CNFs

The synthesis of Al_2O_3 coating on CNFs was conducted by using a condensed layer deposition (CLD) [67, 68]. In brief, the CNFs were surface treated by a mixture of sulfuric acid and nitric acid at a volume ratio of (3:1) at a concentration of 6.0 (mole/L) under a sonication force for 2 hours at 60°C followed by deionized water washing to remove any left-over acid. The coating process was done as follows: each batch of 400 mg of CNF was dispersed in 500 ml heptane in two containers (200 mg in 250 ml each). After a 20-minute period of sonication, 150 micro-liters of water added to the mixture under both forces sonication and stirring. After another 20 minutes, the water film is formed on the CNFs surface. Afterward, a 0.00789 mole of the TMA based on the reaction $(2TMA + 3H_2O \rightarrow Al_2O_3 + 6CH_4)$ was injected under a nitrogen blanket to prevent any atmosphere effect. The samples were dried under vacuum at 100°C for 8 hours. Subsequent annealing to remove any residues in form of CHx was conducted at 350°C for 2 hours under air in a tubular furnace.

2.4 Improper Al_2O_3/CNFs dispersion technique

The first attempt in this research to disperse Al_2O_3/CNFs in the water was done by using 100% of the water that is used to prepare the mortar mixtures. Different ratios of the superplasticizer were added directly to the suspension and many air bubbles were produced in the aqueous solutions as shown in Figure 2.2. When the samples were tested, they exhibited a weak mechanical response. Although the reason is not fully understood, but it could be due to the acidic nature of the superplasticizer. This acidic behavior might have

stripped the coating layer off leading to non-coated CNFs. Further study and careful investigation are needed to gain a better understanding of this behavior.

Figure 2.2 Al_2O_3/CNFs aqueous solutions showing excessive amount of air bubbles during mixing with superplasticizer.

2.5 Dispersion of bare CNFs and Al_2O_3/CNFs and fabrication of mortars

Due to the attraction force represented by Van der Waal's force on the CNFs surface, sonication process for the carbon nanofibers is highly recommended to disperse them in water. The uniform dispersion of the nanomaterials is extremely important to achieve adequate distribution and subsequently effective reinforcement within the composite [69]. Poor dispersion can lead to the formation of defect in the matrix and limit the nano-enhancement/modification effect. Sonication using a probe is highly effective for processing nanomaterial. For this purpose, a sonication probe at 800 W 20 kHz was used as shown in Figure 2.3. It works to convert the electricity to a mechanical energy in a form of shear stress measured in *Joule per minute*. This shear force capable to overcome the Van

der Waal's forces associated with the nanomaterial and as a result increase the distribution-homogeneity. In a typical procedure, CNFs and Al_2O_3/CNFs suspensions can be prepared by sonicating them in water. This water then can be used as a mixing agent to prepare the composite mortars. Workability or defined as fluidity is a crucial matter to get a uniform mixture which is accomplished by adding a certain ration of a superplasticizer to the mixture of water and nanomaterials or to water only.

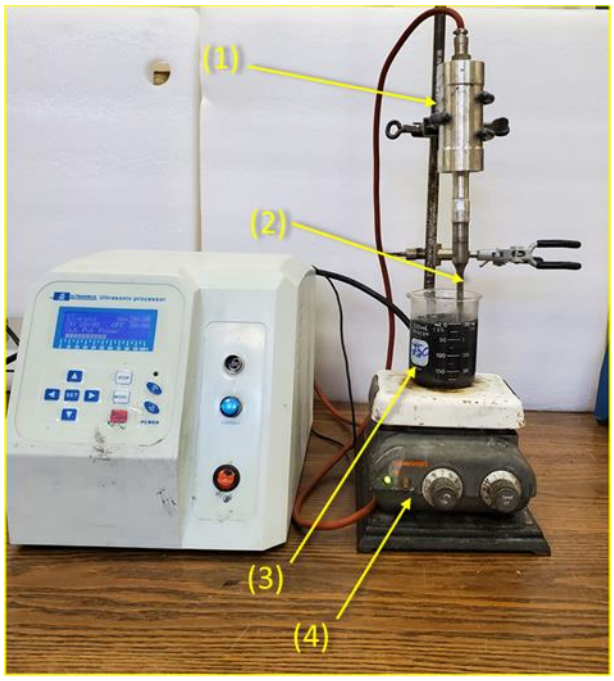

Figure 2.3 Sonication setup showing; (1) Sonicator, (2) Probe diameter size of 10 mm, (3) Al_2O_3/CNFs, or CNFs with superplasticizer suspension, and (4) Hot plate stirrer.

The superplasticizer as a surfactant was used only with the suspensions that had CNFs. A constant cement-to-sand ratio of 1:2 and water-to-cement ratio and of 0.35 was used, respectively. Three different ratios of CNFs and Al_2O_3/CNFs (0.125 wt.%, 0.25 wt.%, 0.5 wt.%) were prepared, in addition, a control specimen without addition of nanomaterial denoted as (C0) was prepared. The mixing properties are listed in Table 2.3. In case of Al_2O_3/CNFs, 80% percent of water was used for dispersion and 20% was mixed with

superplasticizer. The suspensions were simultaneously sonicated and mixed with a mechanical stirrer at room temperature for 30 minutes. Later, the suspensions were added to the cement and sand for 3 minutes mixing using Hobart mixer as in Figure 2.4. Figure 2.5 illustrates the coating steps and the mixing procedures for Al_2O_3/CNFs composites. Afterward, the fresh mixture was cured and cast into different molds for different testing procedures described in this thesis.

Figure 2.4 Al_2O_3/CNFs or CNFs suspension pouring during mixing with cement and sand.

Table 2.3 Mixing proportions recipes and nanomaterials contents

Sample designation	Mix proportion (wt.%)					CNFs content (wt.%) *
	Water-cement ratio (w/c)	Sand-cement ratio (s/c)	CNFs	Al_2O_3/CNFs	Superplasticizer	
C0	0.35	2	-	-	0	-
CNF-0.125	0.35	2	0.125	-	0.1	100
CNF-0.25	0.35	2	0.25	-	0.2	100
CNF-0.5	0.35	2	0.5	-	0.4	100
Al_2O_3/CNF-0.125	0.35	2	-	0.125	0.1	58
Al_2O_3/CNF-0.25	0.35	2	-	0.25	0.2	58
Al_2O_3/CNF-0.5	0.35	2	-	0.5	0.4	58

*Data obtained from TGA analysis shows the mass of CNFs in Al_2O_3/CNFs composites

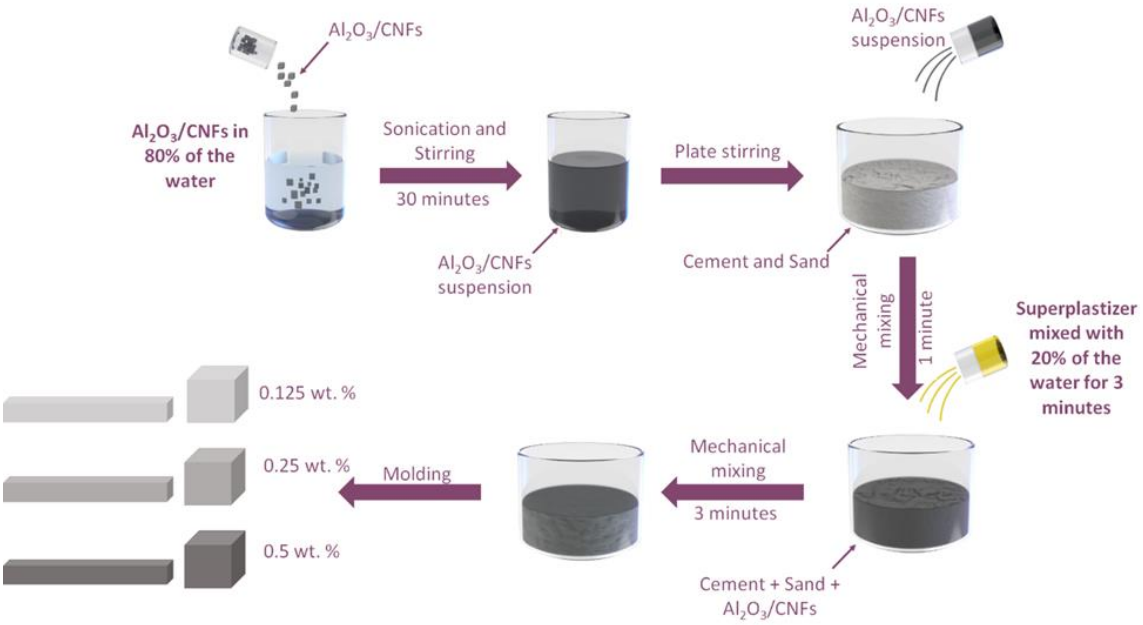

Figure 2.5 A cartoon displays the steps of cement mortars preparation when the Al_2O_3/CNFs used.

2.6 Characterizations

In this section, two types of morphology characterizations and their associated scopes were demonstrated. The TEM scope was used for detecting the nanocoating of Al_2O_3 on the CNFs. Another scope was used is the SEM for the cement material specimens. The SEM was coupled with EDS for further quantification characterization.

2.6.1 Transmission electron microscopy (TEM)

The nanocoating of aluminum oxide on the CNFs was characterized by using transmission electron microscopy (TEM) scope. The JEOL JEM-1400 equipped with Lanthanum-hexaboride (LaB6) filament was operated at an acceleration voltage of 120 kV and data were collected on the Gatan Ultrascan 1000 CCD camera, shown in Figure 2.6 below. The TEM is crucial to detect the nanocoating morphology and its distribution as well as the coating efficiency.

Figure 2.6 JEOL JEM 1400 located in the electron microscopy core facility at the University of Missouri.

2.6.2 Scanning electron microscopy (SEM)

Scanning electron microscopy (SEM) is a surface imaging technique capable to capture nanometer resolution on topographical features. In other words, SEM (Figure 2.7) is a focused electron beam over a sample surface to create an image. It is a strong and feasible technique used to study the microstructure and chemical compositions of cementitious materials with a high spatial resolution up to micron scale by examining the cement hydration products. Two types of signals are usually detected, the backscattered electron (BSE) and the secondary electron (SE). There is a distinct difference between the two SEM imaging modes. The SE is a low energy (<50 eV) as it is produced on the surface. It is not exceeding a couple of nanometers underneath the sample surface. Therefore, the detected signal is attributed to those escaped electrons from the surface. On the other hand, backscattering possesses a high electron energy that penetrates a couple of microns within the sample. The BS is a functional tool for identify the sample elements in particular the heavy materials (high Z material). The SE becomes ideal when the user has a fracture surface rather than a smooth flat topography [70]. In this thesis, the SE was used to study the microstructure of the cements mortars specimens for the CNFs-0.5 and Al_2O_3/CNFs-0.5 samples. The SEM specimens were prepared by using the cracked residue from the cubic specimens that experienced a compressive test directly without any further treatment at the age of 28 days.

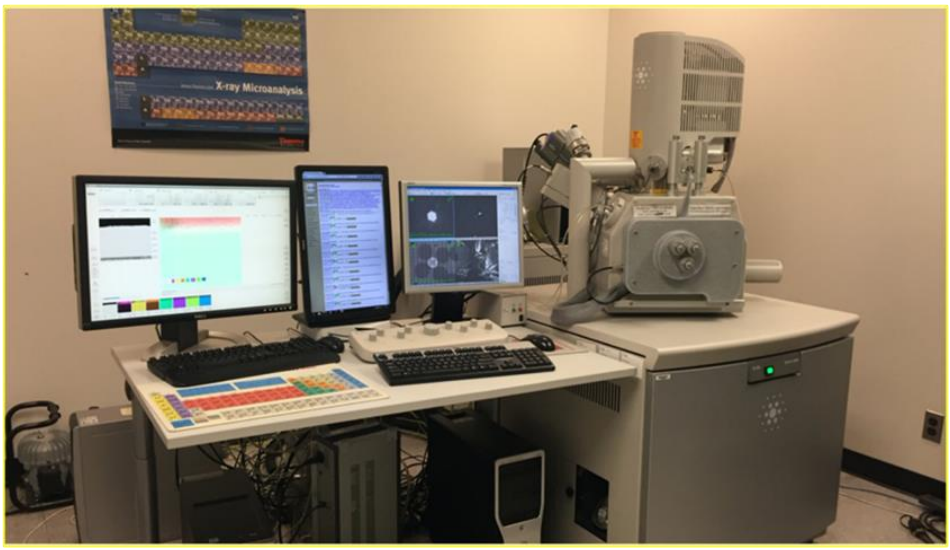

Figure 2.7 FEI Quanta 600 FEG SEM scope located in electron microscopy core facility at the University of Missouri.

2.6.3 Energy dispersive X-ray spectroscopy (EDS)

This technique is useful for chemical characterization of a sample in combination with SEM. This characterization is for the near-surface elements and their amounts at different positions providing a map of the sample. In brief, it works as the sample is hit by the electron beam. Some electrons in different energy levels (such as K, L) are ejected creating electron vacancies. Afterward, those ejected electrons are compensated by electrons from a higher energy level state. This transfer is associated with the X-rays emitted to balance the energy difference between the two electrons energy levels states. This method is technically an explicit process to identify the elements because each single atom of elements has its unique energy levels values. Therefore, EDS has been used to determine the main compositions of the Portland cement reinforced by different nanomaterials qualitatively [71]. The EDS has also the ability to scan a descent area of the sample to spot the location of interest. After finding the location of interest, EDS can generate a spectrum

which can provide the percentage of each element in the selected location. By scanning multiple locations, EDS can give a sense on how the nanomaterials are distributed, how much, and where the hydration products (such as CH, C-S-H, C-A-H, C-A-S-H) are located [72]. In this research, the samples were prepared by taking a small amount of the material in a disc-like mold after 28 days of age; see Figure 2.8. The disc samples were characterized by FEI Quanta 600 FEG SEM scope.

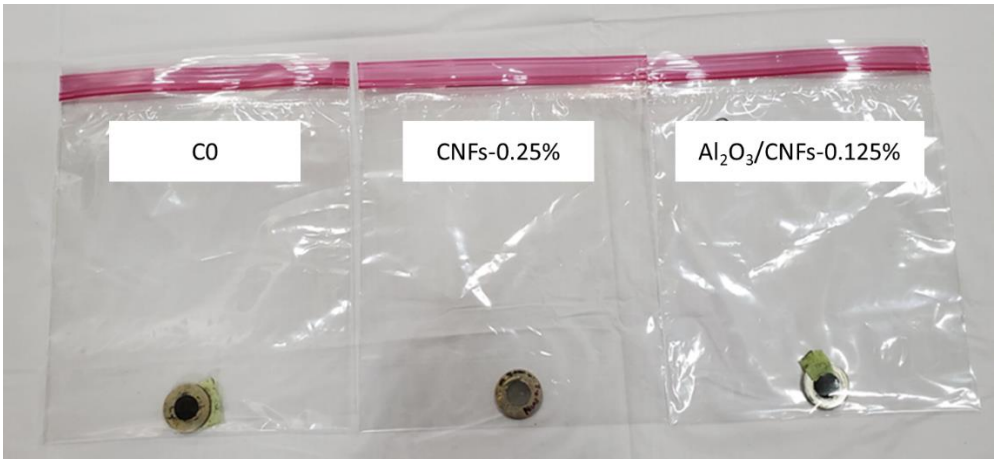

Figure 2.8 Preparation the samples for EDS analysis inside a washer disc.

2.7 Thermogravimetric analysis (TGA)

Thermogravimetric (TGA) and differential thermogravimetric (DTG) curves were obtained to detect the influence of CNFs and Al_2O_3/CNFs in the hydration reaction of cement mortars at a water/cement ratio (w/c) of 0.35. In general, the decomposition of cement hydrates can be divided into three major regions. The first peak between 25 and 400°C represents the evaporable water and dehydration of hydrated calcium silicate (C-S-H). The second one which is located between 400 and 600°C represents the dehydroxylation of portlandite (CH). The last peak due to decarbonation of $CaCO_3$ is located between 600 and 800°C [73]. Nine samples with dimension of 50×50×50 mm at

w/c of 0.35 were prepared for the TGA testing. The samples were taken out of the lime water on the day prior to the TGA test. Then they were left for 24 hours to dry in a fume hood. In the second day, the samples underwent a compressive strength test to reach their cores. Samples for the TGA testing were obtained at and age of 7, 14 and 28 days. No special treatments, like drying or pouring in any solvent, were used to avoid the effect of the carbonation on the results [74]. Cement mortar slices in the size of 5-8 mm were taken from the core of the cubic samples. The slices were crushed to powders and filtered by passing through 75-µm sieve. Thermal analysis (TGA) model Q-500 was conducted in a range of 25-1000°C by a scan rate of 10°C/minute under nitrogen gas. The setup of TGA analysis is shown in Figure 2.9.

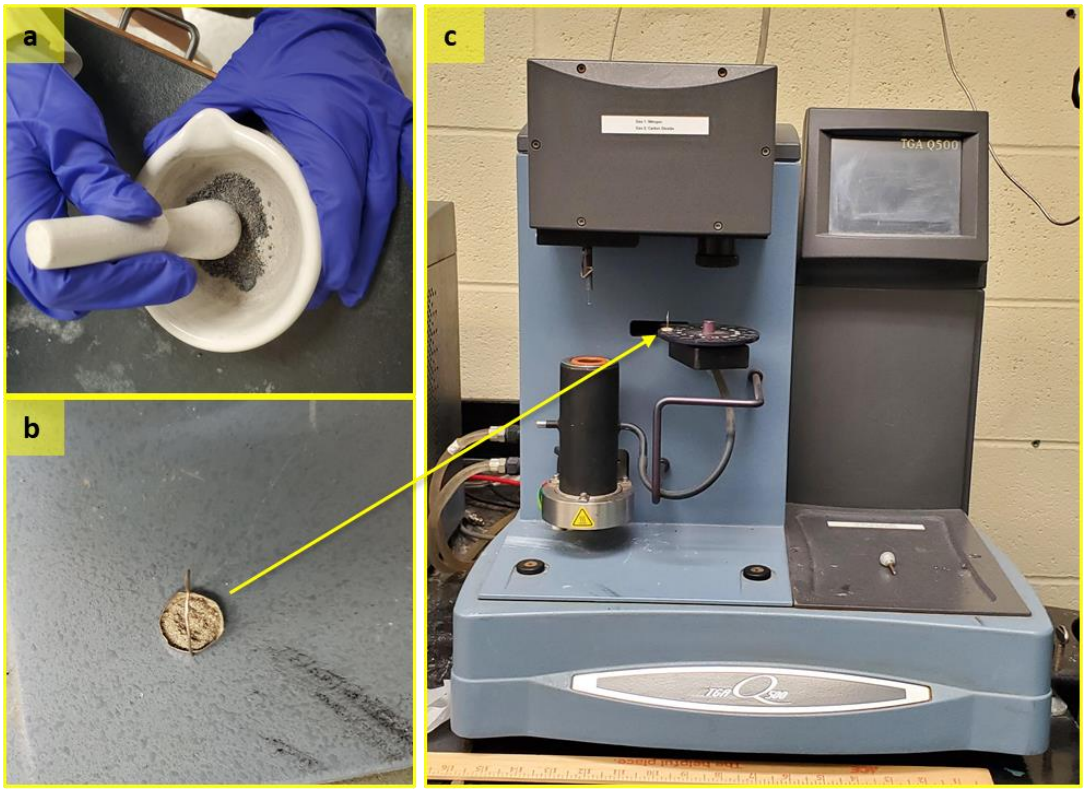

Figure 2.9 Sample preparation for TGA (a) Grinding the cement, (b) Alumina pan holds 23 mg of the powder, (c) TGA (Q-500)

Two important parameters, the degree of hydration (DOH) and calcium hydroxide content were obtained from to the TGA results. The first parameter was estimated using the method suggested by Pane et al. [75]. The weight loss between 140°C and 1000°C was considered as the weight of chemically bound water (CBW) and the degree of hydration for the samples was calculated using the equation below:

$$\sigma = \frac{w_{140} - w_{1000}}{w_0 \times 0.23}$$

Where σ is the degree of hydration, W_{140} and W_{1000} are the weight of samples at 140°C and 1000°C, respectively; W_0 is the initial weight of the sample, and the factor 0.23 is the weight of the non-evaporable water content per unit gram of un hydrated sample.

The amount of portlandite (CaOH) was also related to the degree of hydration and pozzolanic rate of the cement composites. The below formula can be used to determine the quantity of the CH.

$$M_{CH} = \frac{MW_{CH}}{MW_H} \times W_{CH}$$

$$M_{CH} = \frac{74}{18} \times W_{CH}$$

Where W_{CH} is the percent weight loss of portlandite (CH), MW_{CH} is the molecular weight loss of CH, and MW_H is the molecular weight of H_2O.

2.8 X-ray powder diffraction (XRD)

X-ray diffraction (XRD, Philips X-pert) equipped with Cu Kα was performed to analyze the crystalline phase of the samples. The data was collected over an angle range of 2θ = 5° – 90° at a scan rate of 0.026° s^{-1}. The samples (50 mg in weight) were grained and sieved by a 75 μm sieve.

2.9 BET and pore volume measurements

The specific surface area of different powders was calculated by Brunauer-Emmett-Teller (BET) analysis method using a surface area analyzer (Beckman Coulter SA 3100). The data was collected based on nitrogen adsorption-desorption. Briefly, 225 mg of the cement that has a diameter $d \leq 300\mu m$ was degassed at 200°C for 180 minutes. After the degassing, the mass was recorded to be ~180 mg for the three samples C0, CNFs-0.25%, and Al_2O_3/CNFs-0.125%. The Barrett-Joyner-Halenda (BJH) mode was used to collect the pore size distribution of the samples.

2.10 Mechanical characterizations

The compressive strength was determined following ASTM C109_standard [76]. Sixty-three specimens in dimensions of 50 mm × 50 mm × 50 mm were tested. For consistency purposes, all the tests were conducted at room temperature of 22 ± 3℃. After unmolding of the specimens, they were placed in saturated lime water at 23°C in a moist room. By the testing step time, the specimens were removed from the lime water container and then were wiped with cloth for drying purpose. The specimens at 7, 14, 28 days, were tested by applying the load to specimen sides that were in contact with the true plane surfaces of the mold. A load is applied at the rate of 300 lb/s uniformly until the specimen is deteriorated at a certain peak where the compressive strength is recorded. The compressive strength is calculated based on the equation below:

$$f_m = \frac{P}{A}$$

Where, f_m = compressive strength of specimen (Pa), P = maximum peak load at failure of specimen in (N), and A = area of cross section in (mm^2)

For reliability, the collected data was averaged for three samples for all mortar composites specimens C0, CNFs, and Al_2O_3/CNFs. The loading setups for the compressive strength test shown in Figure 2.10.

Figure 2.10 Compressive strength test apparatus (Forney machine).

2.11 Workability (fluidity)

Fluidity or workability testing was performed to evaluate the effect of the addition of Al2O3/CNFs and CNFs on the cement mortars. Fluidity of different composites mixtures were examined based on ASTM C1437-13 standard [77]. After the mixing process, a specific amount of each mixture was poured into the flow table to test the workability. The flow mold that has bottom base with 100 mm wide and a top surface of 70 mm in diameter was placed in the center of the cleaned and dried flow table (see Figure 2.11). The mortars of 7 different mixtures were placed in the mold in two layers. Each layer was compacted 20 times until a flat and smooth top surface was obtained. After removing the flow mold, the flow table was dropped 25 times in less than 20 seconds. The final diameters were recorded to calculate the mixture flow diameter by recording the diameter along four directions.

Figure 2.11 Flow table apparatus

2.12 Freeze-thaw testing

The test for measuring the frost resistance of mortar composites reinforced by CNFs and Al_2O_3/CNFs at different ratios was performed based on ASTM C666 standard [78]. In this standard, two methods were outlined, procedure A, which conducts the freeze and thaw cycles in water and procedure B, where the freezing of the sample is in air and the thawing is in water. In this study, procedure A was followed by using an automated freeze-thaw chamber (Figure 2.12), where the samples were submerged in water and the temperature of the water is automatically adjusted with a timer to achieve each freeze-thaw cycle. The process was conducted at a temperature range of -18°C to 4°C (Figure 2.13). Each cycle was conducted in 2-5 hours with a minimum of 25% of cycle time is to be for thawing.

Before the freeze-thaw test, specimens were prepared and cast in prism molds with dimensions of 25 mm × 25 mm × 280 mm. Based on ASTM C666 standard, the minimum width and height should be 75 mm but due to limitations of the nanomaterials (especially for the coated CNFs), prism with a height and a width of 25 mm was used [23]. Then the specimens were demolded and moist-cured for 28 days, to allow them to gain strength before placing them into the freeze-thaw chamber.

After curing and before placing in the freeze-thaw chamber, the mass of the specimens was measured and recorded. The day of the test event is after 28 days for all the samples. The samples were subjected to at least 300 freeze-thaw cycles. For the specimens with optimum dosage of nanomaterials, 0.125 for Al_2O_3/CNFs and 0.250 for CNFs, compressive strength and mass were measured at an interval of 50 cycles. The compressive strength degradation and mass percent change were calculated from the observations at the end of the test. Also, the physical appearance of all samples was recorded after 50, 150 and 300 cycles to observe the damage or the surface scaling changing during their exposure to the freeze-thaw cycles. In this thesis, the percentage length change was not measured. Figure 2.12 presents shows the freeze-thaw chamber and specimens inside the chamber during a freezing cycle, and Figure 2.13 shows the temperature controls of the chamber. The mass loss ratio was calculated using the following equation:

$$\Delta M = \left(1 - \frac{M_n}{M_0}\right) \times 100\%$$

Where ΔM is the mass loss ratio of specimen after the exposure to the freeze-thaw cycling, M_0 is the mass of the specimen before the freeze-thaw cycling, and M_n is the mass of the

specimen after exposure to n freeze-thaw cycles. The compressive degradation, defined as Δf was estimated by the following equation:

$$\Delta f = \left(1 - \frac{f_n}{f_0}\right) \times 100\%$$

Where f_0 is the compressive strength (MPa) of specimen before the freeze-thaw cycling and f_n is the compressive strength (MPa) of specimen after n freezing-thawing cycle.

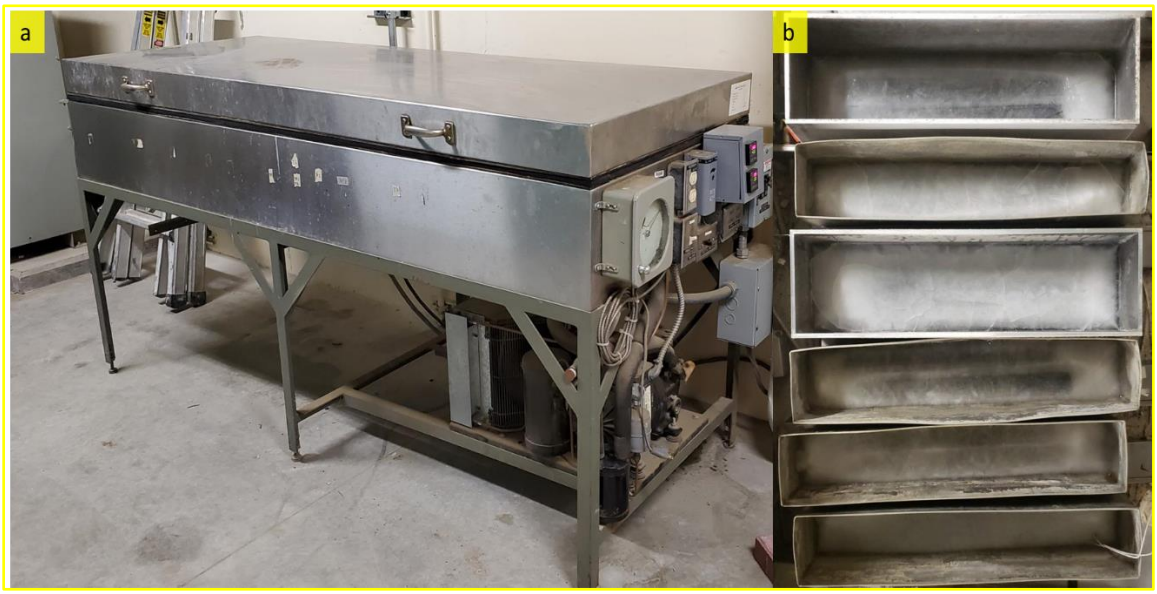

Figure 2.12 (a) Freeze-Thaw cycling test apparatus. (b) Samples under freezing conditions.

Figure 2.13 Freeze-thaw chamber temperature set range of 18°C to 4°C (0°F to 40°F)

2.13 Drying shrinkage

The factors that can influence the shrinkage behavior include temperature, relative humidity (RH), raw cementitious material properties, and volumetric size of the specimens. These parameters need to be fixed during all tests to avoid their effect on the results. Mortar (w/c = 0.4) samples with dimensions of 25 mm × 25 mm × 280 mm were used for drying shrinkage measurements in accordance with ASTM C157/ C157M-17 standard [78]. The molds were purchased from Certified MTP company and its meet the ASTM C490/C490M-17 requirements [79] as presented in Figure 2.14 (b). The mixtures of each patch were placed in the mold in two layers. After casting each layer, the molds were vibrated to ensure adequate compacting. After casting, the molds were placed in suitable zipper bags to ensure the moisture will not escape out of the specimens. Samples were demolded 48 hours after casting and were placed in lime water. At the age of 72 hours, the specimens were removed from lime water and the initial dial gauge readings were taken

immediately. Then the specimens were stored in a dry room of a 22±4ºC and 90% RH. Based on ASTM C157/ C157M-17, the specimens need to be cured for 24 hours, this was not possible for some mixtures that need to cure for at least 48 hours to gain more strength before the demolding due to the high ratio of SP. Therefore, the procedure in curing and taking the length measurements was conducted based on ASTM C596 standard [80]. The length change measurements were taken at ages of 5, 7, 14, 28, and 56 days. The length measurements were taken using length comparator, Figure 2.14 (a), according to the ASTM C490/C490M-17. The average of two samples was taken as the representative value. The setup of the drying shrinkage test is shown in Figure 2.14.

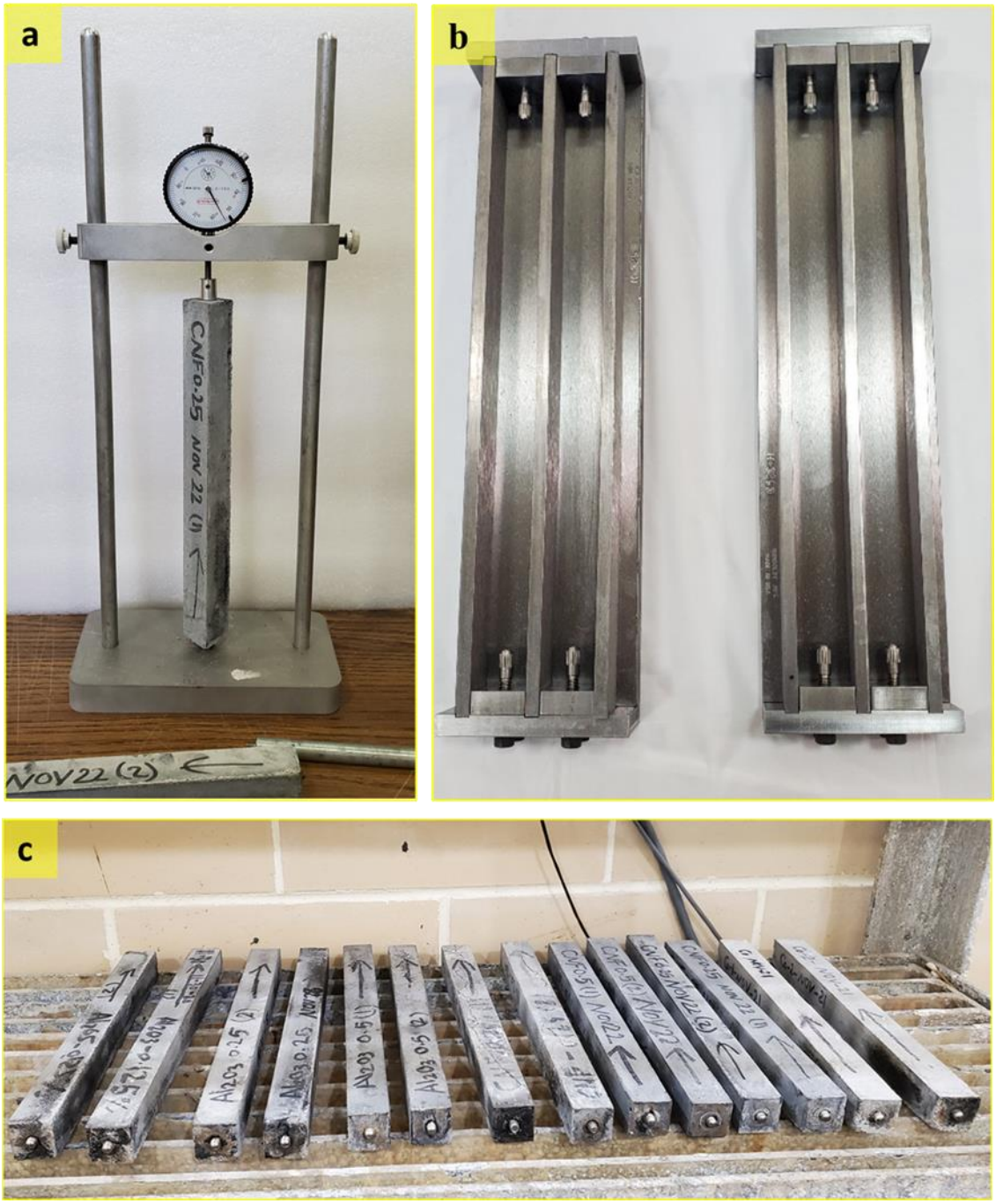

Figure 2.14 (a) Length comparator and dial gauge, (b) Steel prism molds of dimensions 1"×1"×10", 2-Gang. (c) Cement mortar prisms samples in controlled-humidity room.

Chapter Three: Results and Discussion

3.1 General

This chapter presents the results and discussion of this research project. The dispersion of the nanomaterial in water, the pitfalls, and how it is resolved are described in this chapter. The visual characterization results were documented, including the TEM images for the nanocoating of Al_2O_3 on CNFs. The microstructure analysis by SEM images on the fractured cement surfaces and EDS were also reported. In addition, the degree of hydration of the cement mortars were quantified using two independent approaches, namely TGA and XRD, and their results were comprehensively demonstrated. Compressive strength evaluation of the cement composites before and after the freeze-thaw cycles are included in this chapter. A detailed section containing the results of the mass loss and surface appearance is reported. Lastly, the results for fluidity of the cement mortars, the drying shrinkage, pore structure are all documented in this chapter.

3.2 Dispersion of bare CNFs and Al_2O_3/CNFs

Figure 3.1 shows a photograph of aqueous CNFs suspension prepared for visual examination of dispersion in water and stability before and after surface functionalization. It also shows the aqueous Al_2O_3/CNFs suspension before and after the annealing at 350ºC under air. After sonicating process of 20 mg in 15 ml of deionized-water (DI-water) for 30 minutes without addition of any surfactant, and the different solutions were left for 30 days. It is seen that the untreated CNFs show no dispersion at all. While the treated CNFs show a relatively good dispersion to the untreated one. But after 30 days, the CNFs clusters are clearly visible at the bottom of the vials. The fresh Al_2O_3/CNFs shows a quick settlement

which is due to the organic ligands left over from the coating precursor molecule. The scenario is totally different after the fresh Al_2O_3/CNFs was exposed to air at a temperature of 350ºC for one hour. Therefore, it clear that annealed Al_2O_3/CNFs suspensions had much better long-term stability as compared with other suspensions. This can be attributed to the formation of pores due to the oxidizing of the organic content converting Al_2O_3/CNFs to result in a highly hydrophilic surface.

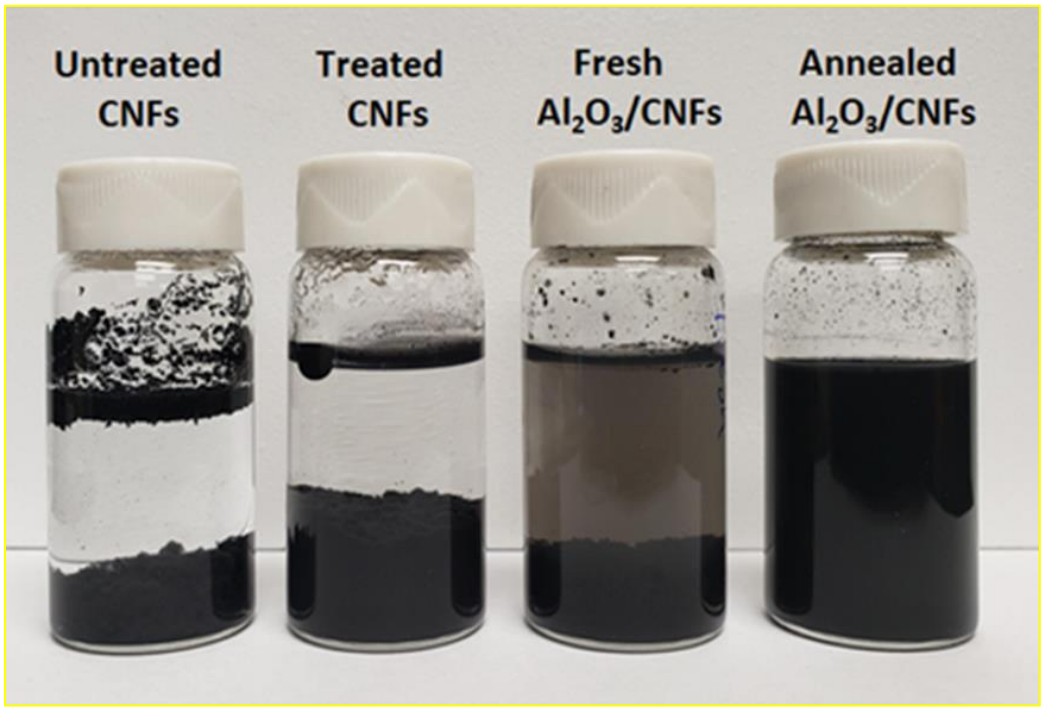

Figure 3.1 CNFs and Al_2O_3/CNFs dispersion in water after one month.

3.3 Characterizations results

This section presents the results of the TEM images of the nanocoating and the SEM images of the microstructure of the cement mortars specimens. The EDS elementals mapping and the element spectrum on the samples were also included.

3.3.1. Transmission electron microscopy (TEM)

The nanocoating of Al_2O_3 on CNFs was characterized by TEM in both low and high resolution as seen in Figure 3.2. For comparison, bare CNFs were examined by TEM as well as seen in Figure 3.2 (a). Figure 3.2 (b) shows a uniform coating with a porous morphology which plays a role in the cement hydration. The surface area of the Al_2O_3 nanocoated CNFs was measured by BET to be 274.3 m^2/g as shown in Figure 3.2 (c). To determine the exact Al_2O_3 and CNFs content, TGA analysis shows 42% and 58% weight percent of Al_2O_3 and CNFs, respectively (Figure 3.2 (d).)

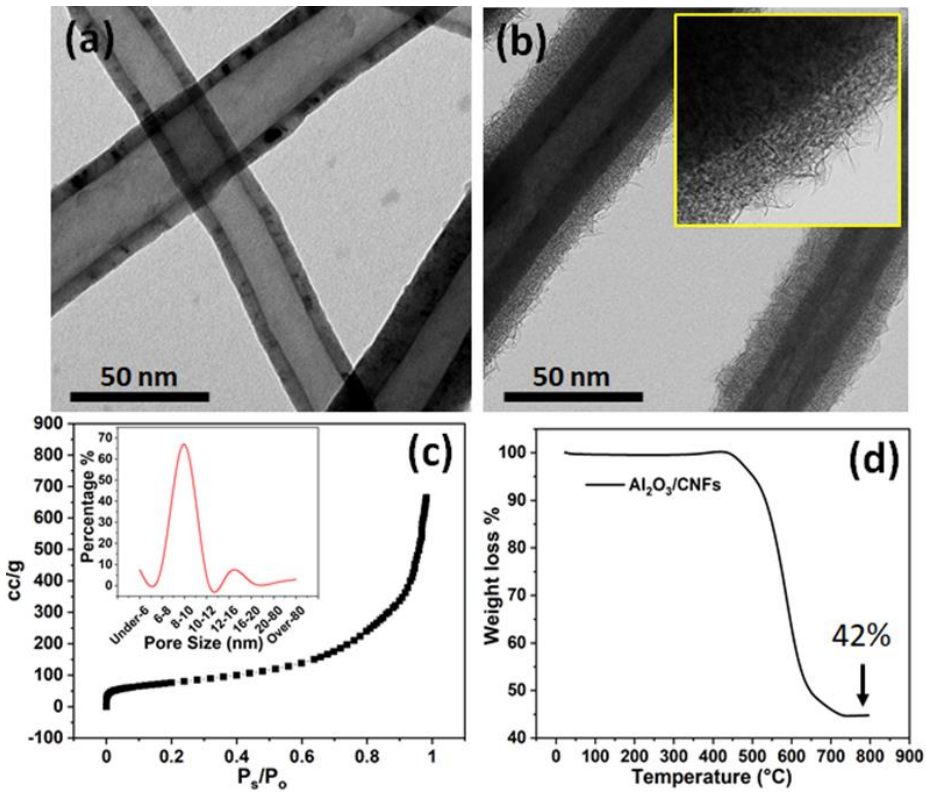

Figure 3.2 Bright field transmission electron microscopy (TEM), (a) TEM image shows the uncoated CNFs, (b) TEM image shows the Al_2O_3 coating on CNFs, the inset shows high magnification TEM image shows the layer morphology, (c) BET analysis for Al_2O_3/CNFs with its

3.3.2 Microstructure analysis

3.3.2.1 Fracture surface microstructure

The microstructure of the cement mortar specimens was characterized by the scanning electron microscopy (SEM). Figure 3.3 shows the SEM images for CNFs and Al_2O_3/CNFs at the age of 28 days, where the hydration products like crystalline CH, needle-shaped ettringite, amorphous calcium-silicate-hydrate (C-S-H) are clearly distinguished. The SEM session was done at a voltage of 5 kV to avoid any surface charging under the beam exposure. Figure 3.3 (a through d) show the CNFs and Al_2O_3/CNFs-embedded cement mortar (marked by arrows). Al_2O_3/CNFs was found to be well anchored in the hydration products and was encapsulated by uniform and compacted C-S-H hydration products. Increasing in the C-S-H gel formation is attributed to the contribution of the Al_2O_3 nanocoating as an effective layer with high surface area that provides preferential nucleation sites for hydration products growth. In addition, based on the observation of the surface morphology, lower CH content was found when comparing with CNFs-mortar composites. This could be due to the consuming of CH formed during the hydration of the cement [49]. On the other hand, the fracture surface for the CNFs composites shows a good interaction with the mortar matrix with lots of CH contents.

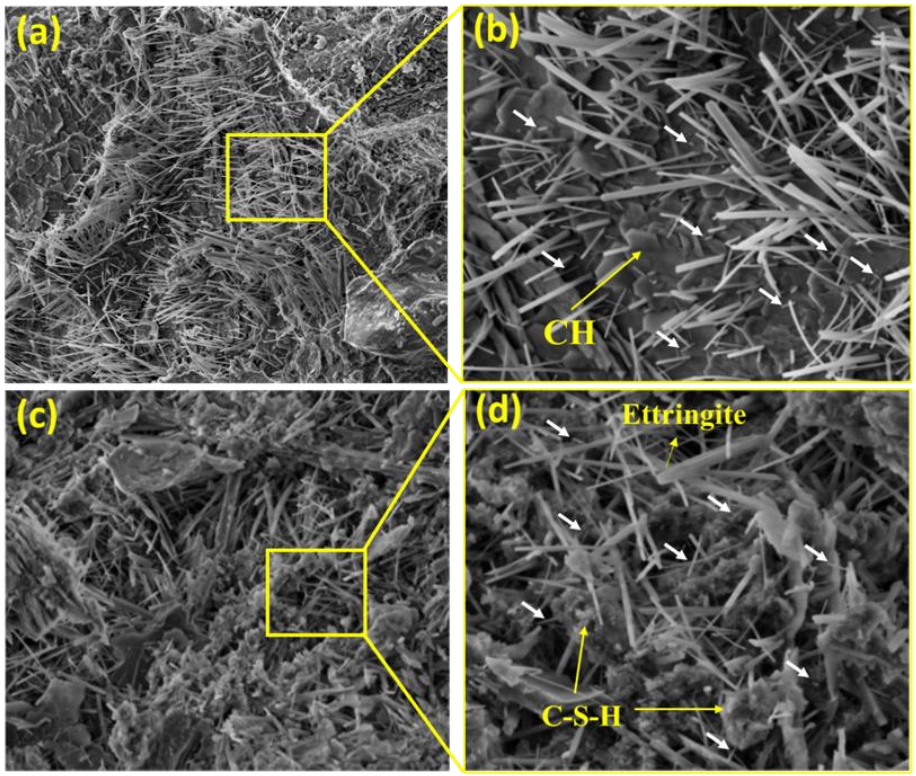

Figure 3.3 SEM images at different magnifications at 5000x and 10000x: (a and b) CNFs embedded cement mortar, (c and d) Al_2O_3/CNFs embedded cement mortar, all at the age of 28 days.

The morphology and microstructure characteristics were able to revel a visual evidence on the ability of the Al_2O_3/CNFs composites to bridge the microcracks. Figure 3.4 shows the micro crack of the control sample. In comparison, the existence of the Al_2O_3/CNFs in the mortar composites worked to bridge the narrow micro cracks. This is an important effect which can restrain the development of the internal micro cracks in mortar matrix, hence better mechanical properties can be obtained.

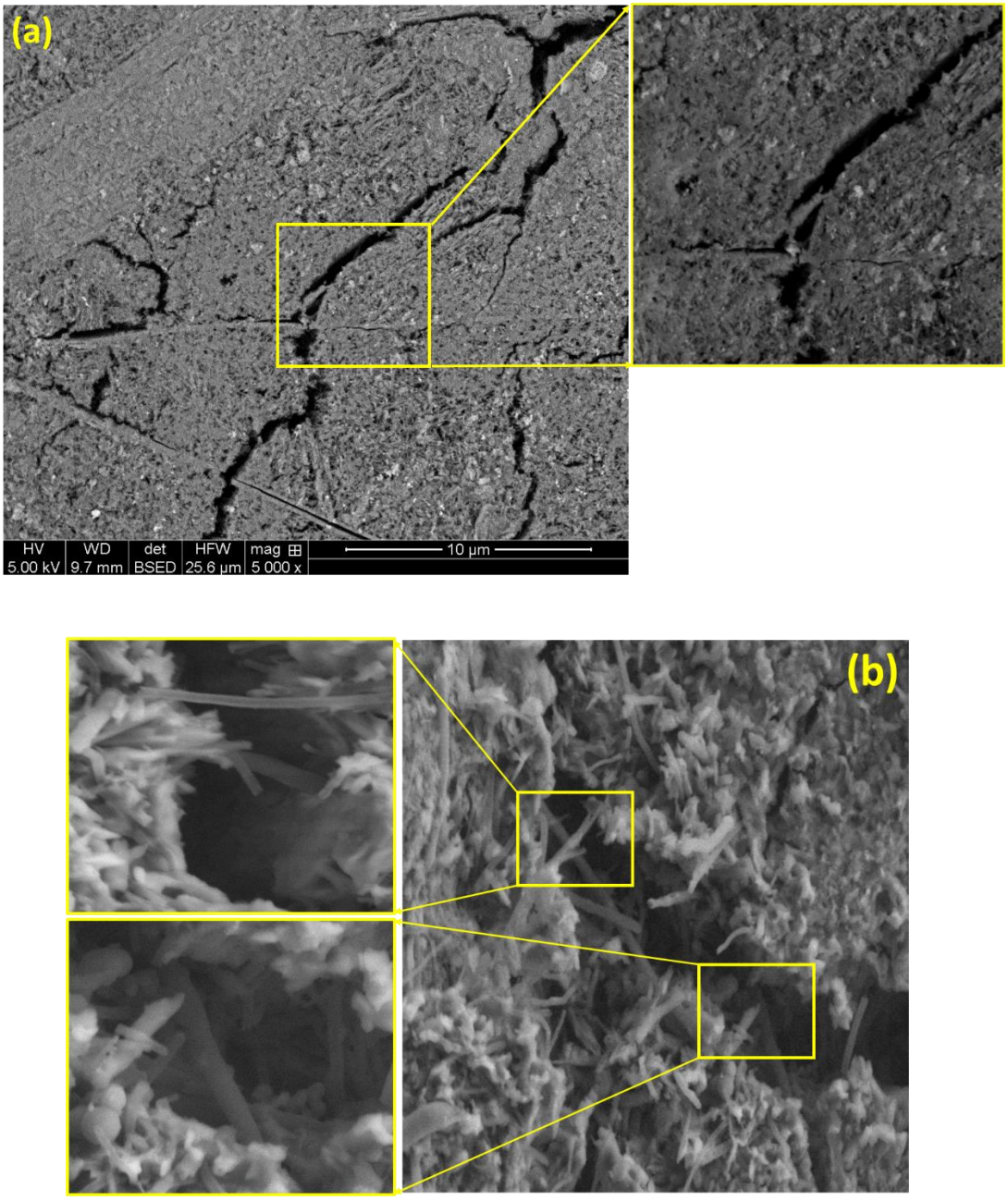

Figure 3.4 Micro cracks in (a) Control sample (C0) at magnification of 5000x, (b) Al_2O_3/CNFs-mortar composites at magnification of 10000x.

3.3.2.2 Energy-dispersive X-ray spectroscopy

The EDS spectrum analysis for the reference sample C0 is shown in Figure 3.5. The ratio of calcium to silicon is shown to be 10.97. This value is used as a metric to determine the consumption of calcium converted to silicate hydrated moiety.

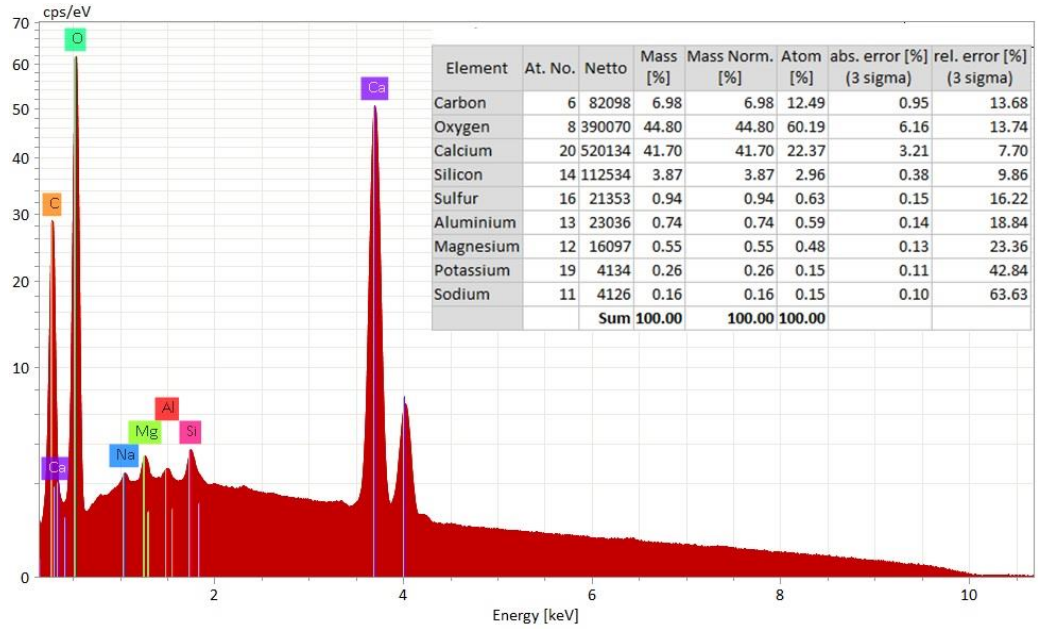

Element	At. No.	Netto	Mass [%]	Mass Norm. [%]	Atom [%]	abs. error [%] (3 sigma)	rel. error [%] (3 sigma)
Carbon	6	82098	6.98	6.98	12.49	0.95	13.68
Oxygen	8	390070	44.80	44.80	60.19	6.16	13.74
Calcium	20	520134	41.70	41.70	22.37	3.21	7.70
Silicon	14	112534	3.87	3.87	2.96	0.38	9.86
Sulfur	16	21353	0.94	0.94	0.63	0.15	16.22
Aluminium	13	23036	0.74	0.74	0.59	0.14	18.84
Magnesium	12	16097	0.55	0.55	0.48	0.13	23.36
Potassium	19	4134	0.26	0.26	0.15	0.11	42.84
Sodium	11	4126	0.16	0.16	0.15	0.10	63.63
		Sum	**100.00**	**100.00**	**100.00**		

Figure 3.5 EDS spectrum and elements mass percent for C0.

The EDS-elementals mapping results of Al_2O_3/CNFs-0.125% are displayed in Figure 3.6. It is seen that the elements are well-distributed with minimal aggregation. The carbon signal is subtle, which is reasonable as there is only 0.125% of the nanomaterial of Al_2O_3/CNFs. Out of 0.125 wt.%, there is only 58% as CNFs, which give a net CNFs percentage of 0.0725 wt.%. Aluminum signal seems to be strong which is due to the original presence of Al in the cement mortar or may be coming from the secondary C-A-H gels.

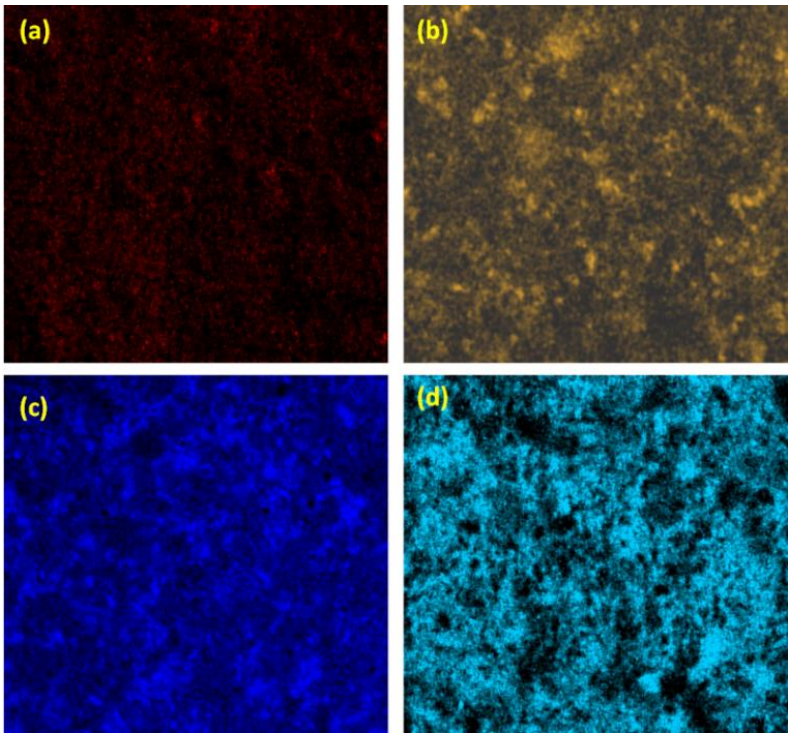

Figure 3.6 Elementals mapping from X-ray for a selective area of the cement mortar of Al_2O3/CNFs-0.125% (a) C, (b) Al, (c) Ca, (d) Si.

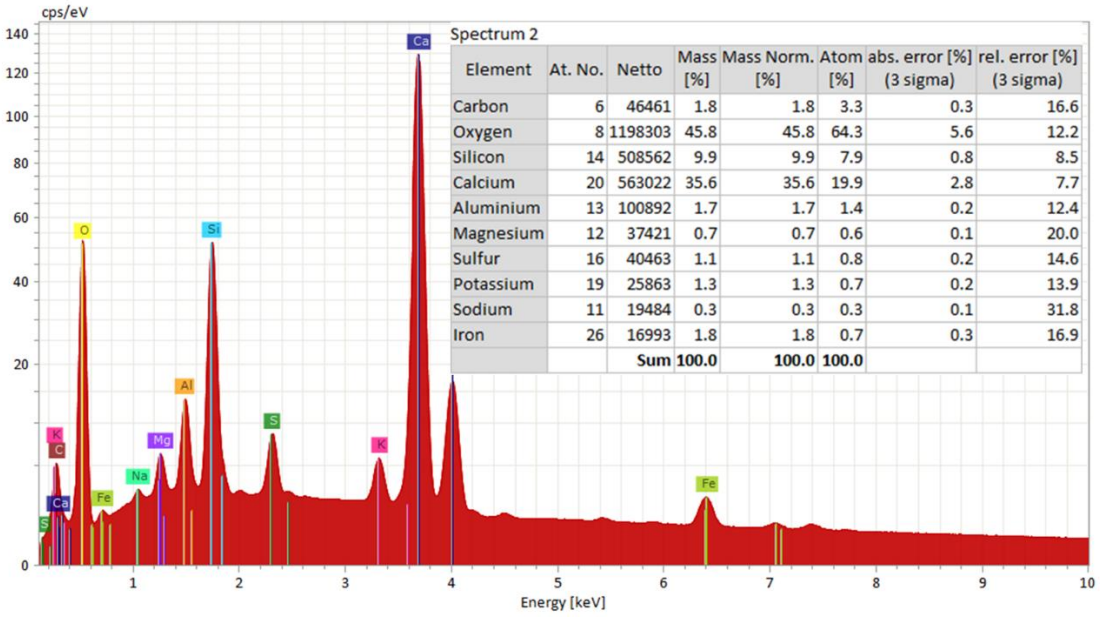

Element	At. No.	Netto	Mass [%]	Mass Norm. [%]	Atom [%]	abs. error [%] (3 sigma)	rel. error [%] (3 sigma)
Carbon	6	46461	1.8	1.8	3.3	0.3	16.6
Oxygen	8	1198303	45.8	45.8	64.3	5.6	12.2
Silicon	14	508562	9.9	9.9	7.9	0.8	8.5
Calcium	20	563022	35.6	35.6	19.9	2.8	7.7
Aluminium	13	100892	1.7	1.7	1.4	0.2	12.4
Magnesium	12	37421	0.7	0.7	0.6	0.1	20.0
Sulfur	16	40463	1.1	1.1	0.8	0.2	14.6
Potassium	19	25863	1.3	1.3	0.7	0.2	13.9
Sodium	11	19484	0.3	0.3	0.3	0.1	31.8
Iron	26	16993	1.8	1.8	0.7	0.3	16.9
		Sum	100.0	100.0	100.0		

Figure 3.7 EDS spectrum and elements mass percent for Al_2O_3/CNFs-0.125%

From Figure 3.7 (table inset), the amount of Si or Al relative to Ca was determined to decide at what extent the hydration reaction progressed [81, 82]. The same scenario was

carried out on the CNFs-0.25% as in Figure 3.8 and 3.9. The EDS elementals mapping shows well distributed elements. The elementals mapping of CNFs-0.25% cementitious composites have shown more signal of carbon with a minimal Al signal as in Figure 3.8. This is because the sample has more CNFs and has only a trace of Al. On the other hand, the spectrum and the mass percent have shown a different outcome of Al_2O_3/CNFs-0.125%. The Al_2O_3/CNFs-0.125% has shown 3.59 ratio of Ca/Si, however, CNFs-0.25 (Figure 3.9) and C0 have shown a ratio of 4.02, and 10.97, respectively. The higher the ratio the less production of hydration gel products. Therefore, it is thought that the presence of Al_2O_3 induces the formation of the hydration products in the form of calcium-silicate hydrate.

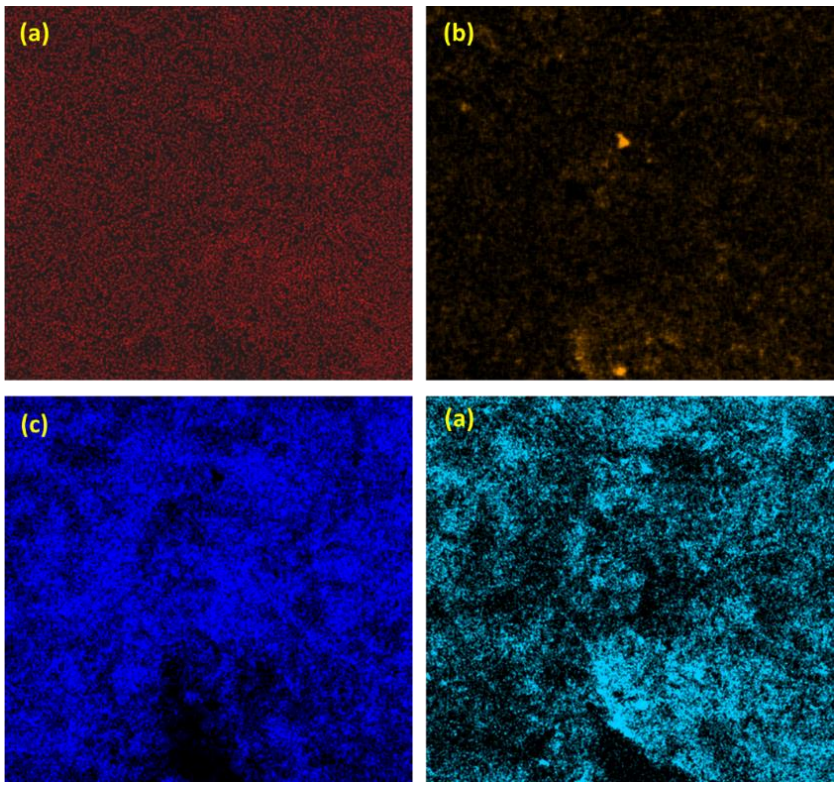

Figure 3.8 Elementals mapping from X-ray for a selective area of the cement mortar of CNFs-0.25% (a) C, (b) Al, (c) Ca, (d) Si.

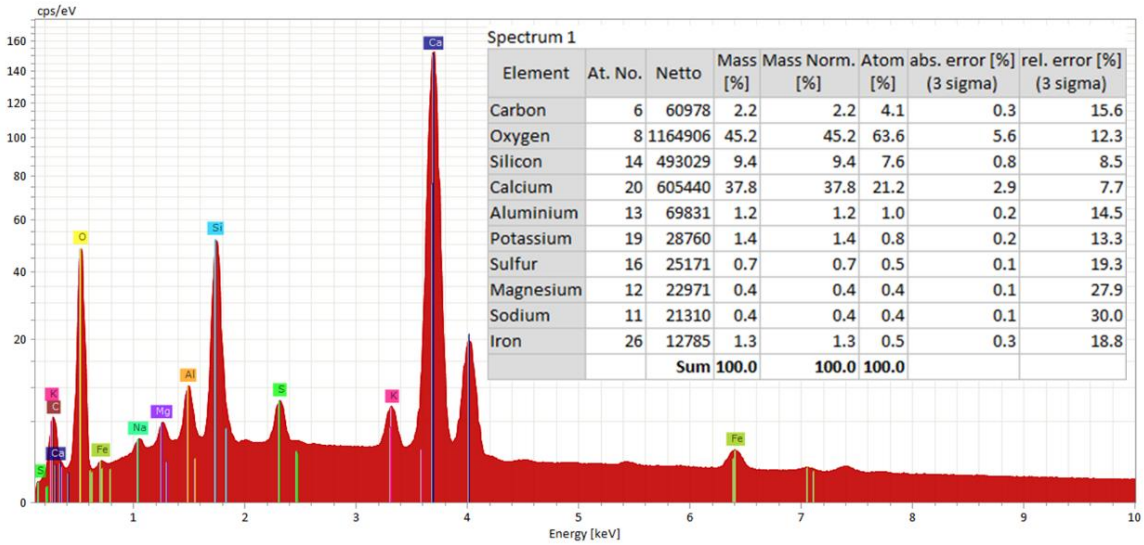

Element	At. No.	Netto	Mass [%]	Mass Norm. [%]	Atom [%]	abs. error [%] (3 sigma)	rel. error [%] (3 sigma)
Carbon	6	60978	2.2	2.2	4.1	0.3	15.6
Oxygen	8	1164906	45.2	45.2	63.6	5.6	12.3
Silicon	14	493029	9.4	9.4	7.6	0.8	8.5
Calcium	20	605440	37.8	37.8	21.2	2.9	7.7
Aluminium	13	69831	1.2	1.2	1.0	0.2	14.5
Potassium	19	28760	1.4	1.4	0.8	0.2	13.3
Sulfur	16	25171	0.7	0.7	0.5	0.1	19.3
Magnesium	12	22971	0.4	0.4	0.4	0.1	27.9
Sodium	11	21310	0.4	0.4	0.4	0.1	30.0
Iron	26	12785	1.3	1.3	0.5	0.3	18.8
		Sum	**100.0**	**100.0**	**100.0**		

Figure 3.9 EDS spectrum and elements mass percent for CNFs-0.25%.

3.4 Compressive strength of composites

The compressive strength results of cement mortars reinforced by CNFs and Al_2O_3/CNFs are presented in Figure 3.10 and Table 3.1. These results are displayed based on the nanomaterials weight percentage at an age of 7, 14 and 28 days. These samples were compared with C0 at all ages. It is observed that with increasing the curing age all samples experienced increase in their strength. The obtained compressive strength varies at all ages with different contents of CNFs and Al_2O_3/CNFs. The compressive strength for samples that contain of CNFs- 0.125, 0.25 and 0.5 wt.% of cement increased by about 15%, 36% and 23%, respectively at age of 7 days. At age of 14 days, the compressive strength of these composites increased by 8%, 23.5% and 14%, respectively. With increasing the curing age of these samples at age 28 days, the improvement of the compressive strength was 5.5%, 15% and 3%, respectively.

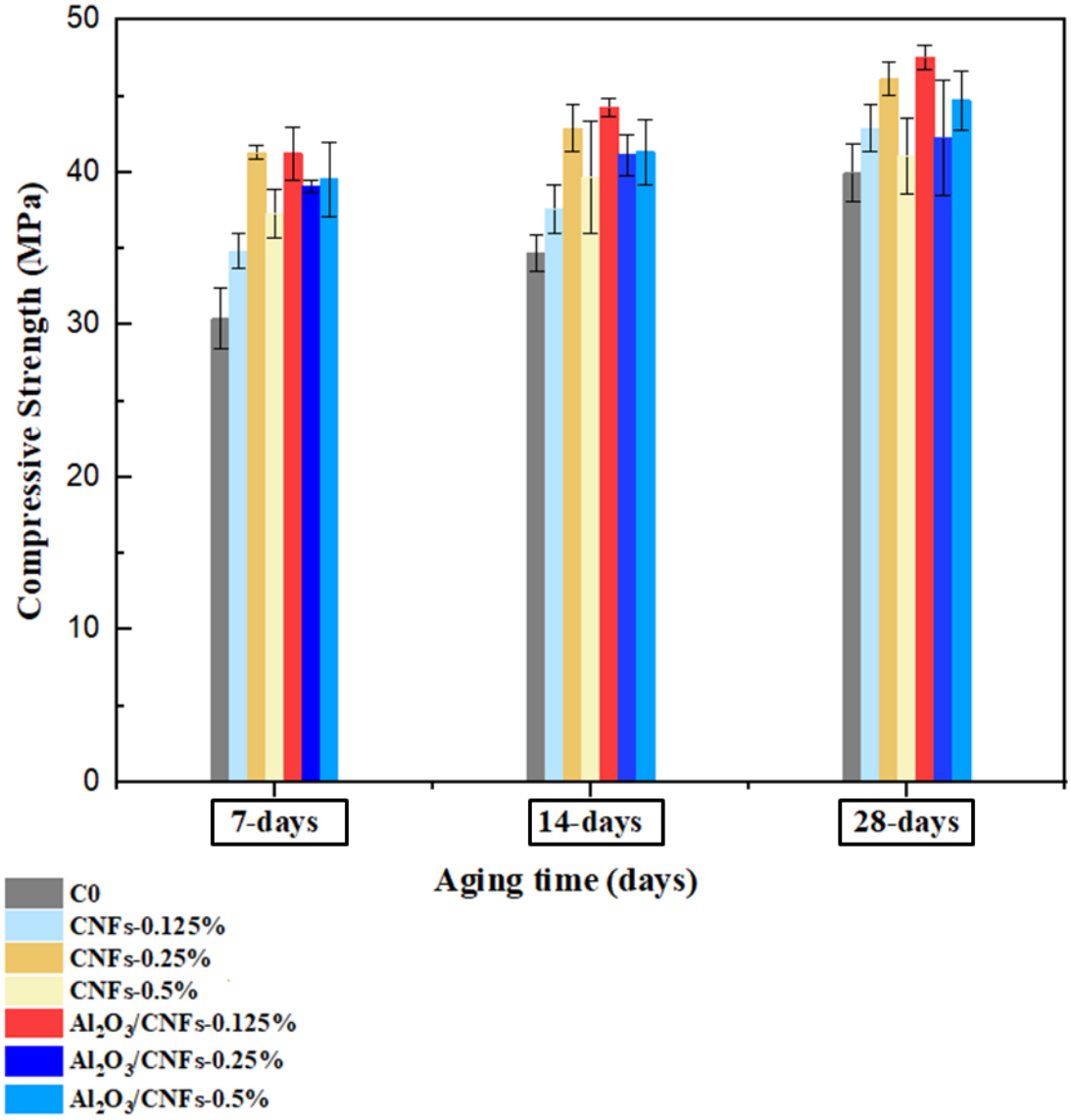

Figure 3.10 Compressive strengths at age of 7, 14, and 28 days for various specimens.

The improvement in the compressive strength with different dosages of CNFs is due to the combined effects of the crack bridging and microstructure densifying due to refining the porosity [40]. Besides, the surface functionalized CNFs possess surface active sites such as (-COOH, -OH, -C=O). These groups have affinity to improve the bonding with Ca^{2+} and to accelerate cement hydration, as a result, improving the mechanical strength [83]. Out of the CNFs samples, CNFs-0.25% has shown high strength due to the structure compacting

and refinement of porosity as shown in Figure 3.11. The filling effect of the CNFs is clearly observed from the SEM images. There was a reduction in the compressive strength when the ratio of the CNFs increased to 0.5%. This can be due to the agglomeration of CNFs inside the cement mortar matrix. The agglomeration creates large cavities which lower the strength [84].

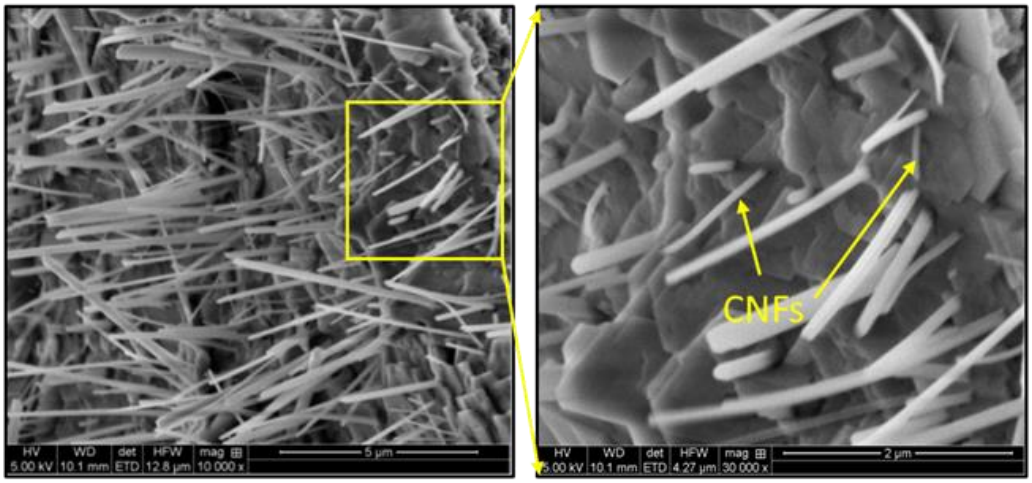

Figure 3.11 Filler effect of the CNFs inside the cement mortar matrix.

On the other hand, the composites that contain the Al_2O_3/CNFs have shown a progressive improvement. Relative to C0, the addition of 0.125 % of the Al_2O_3/CNFs increased the strength by 35.6%, 27% and 19% at age 7, 14 and 28 days, respectively. In case of Al_2O_3/CNFs-0.25 wt.% of cement, the strength exceeded the compressive strength of the control sample by about 28.5%, 18.5% and 6% at age 7, 14 and 28 days. When increasing the dosage of Al_2O_3/CNFs powder to 0.5 wt.% the strength of the samples were increased by 30%, 19% and12%, respectively. The reason behind the good performance of the Al_2O_3/CNFs nanomaterials is the stronger interfacial bonding between the porous layer of the alumina on CNFs with cement matrix. Interestingly, the quantity of the CNFs in Al_2O_3/CNFs was reduced by 42% comparing with 100% of CNFs. The effect of the coating

layer has promoted the mechanical properties of the composites significantly. This layer possesses a highly reactive surface area that promotes the nucleation effect. The reactivity of the surface is defined as high populated active sites that can efficiently adsorb and convert the calcium to calcium-silicate hydrate products. This layer may also contribute to producing extra hydration products which further enhance the pore refinement and densify the cement matrix. In Figure 3.12, one can observe the surface of the coated CNFs (marked with arrows) was encapsulated by the C-S-H hydration product with good interaction between them.

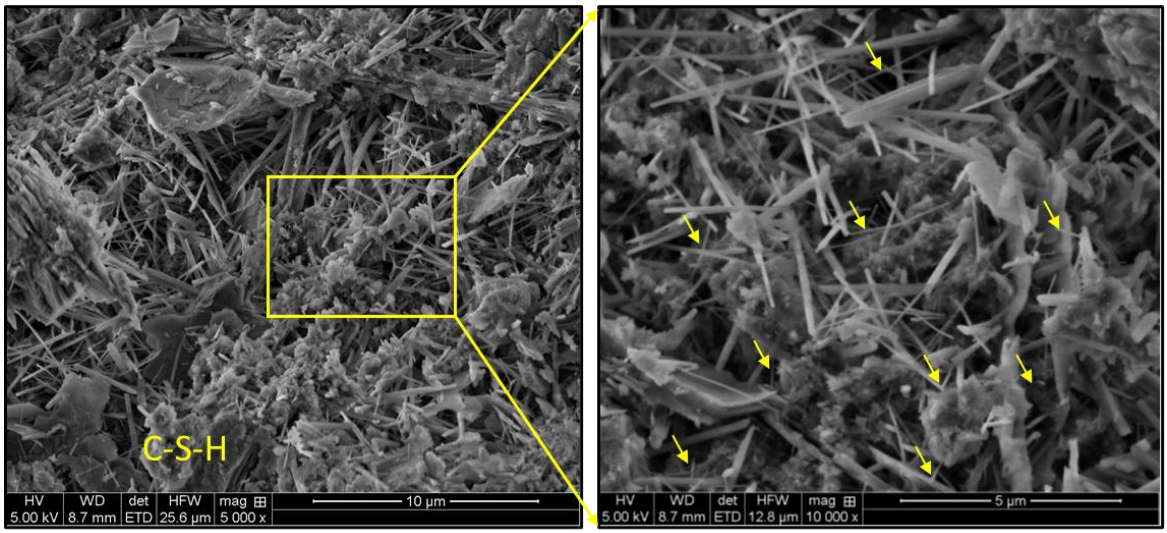

Figure 3.12 SEM images of Al_2O_3/CNFs in mortar composites

Table 3.1 Compressive strength at different curing ages of 7, 14 and 28 days.

Sample designation	SP %	Compressive strength at age 7 days		Compressive strength at age 14 days		Compressive strength at age 28 days	
		Average	S.D.	Average	S.D.	Average	S.D.
C0	0	30.41	2.00	34.73	1.19	39.97	1.85
CNF-0.125	0.1	34.86	1.10	37.61	1.58	42.18	1.89
CNF-0.25	0.2	41.32	0.43	42.91	1.53	46.11	1.10
CNF-0.5	0.4	37.32	1.59	39.67	3.68	41.04	2.48
Al_2O_3/CNF-0.125	0.1	41.23	1.71	44.25	0.63	48.00	4.96
Al_2O_3/CNF-0.25	0.2	39.09	0.44	41.14	1.36	42.26	3.77
Al_2O_3/CNF-0.5	0.4	39.54	2.43	41.36	2.13	44.71	1.94

However, when the amount of the Al_2O_3/CNFs content increased, there was a reduction in the compressive strength. This could be explained as increasing the nanomaterial density in the solution leaves a small distance among the nanomaterials. Also, the excess amount may lead to an inadequate dispersion leading to minimizing the required surface area for the hydration reaction. The mechanism behind lowering the strength might be due to the leaching out the hydration products with no chemical reactivity serving only as fillers. This means there is an optimum percent of the Al_2O_3 and other pozzolan materials to participate in the hydration reaction, which was supported by many studies [85, 86]. In this study, the dosage of Al_2O_3/CNFs-0.125 wt.% was found to be the optimum amount.

3.5 Workability (fluidity)

The effect of the CNFs and Al_2O_3/CNFs with the superplasticizer (SP) on the flow of the cement composites was conducted. The flow table diameter results are presented in Table 3.2. With different percentages of the nanomaterials and SP, the mortar showed different fluidity performance. The C0 fluidity was only 133 mm. The fluidity diameters increased remarkably with the addition of CNFs-SP and Al_2O_3\CNFs-SP at various ratios. However, the fresh mortars reinforced with Al_2O_3/CNFs shows a clear reduction relative to the mortars with different CNFs ratios in flow spread. This reduction in the workability might be assigned to the high-hydrophilic surface area of Al_2O_3/CNFs. This effect of the high surface area demands more water to saturate the surface which reduces the free water in the content [21]. Increasing the dosages of the SP is important to offset the reduction in the fluidity of mortars reinforced with Al_2O_3/CNFs. However, the addition of 0.2% of SP to the mixture that contain Al_2O_3/CNFs-0.25 was not enough to get better workability resulting a lower fluidity among other Al_2O_3/CNFs mixtures. Since the surface area is a function of the mass used, increasing the ratio of these nanomaterials can adsorb more water molecules. This results in a shortage of free water hence the degree of hydration can be affected. And this could explain the lower compressive strength in comparing with other ratios. This has been confirmed by repeating the compressive strength of this ratio two times. However, the SP ratio was not increased to this mixture since the ratio of added nanomaterials to SP needed to be consistent at 1:0.8. This finding was also confirmed by using a thermal analysis at age 7 days for all ratios of Al_2O_3/CNFs composites. The ratio of Al_2O_3/CNFs -0.25% shows lower degree of hydration in comparison with other ratios. These results are not presented in this thesis.

Table 3.2 The slump tests data

Samples	Superplasticizer %	Fluidity(mm)
C0	0%	133
CNFs-0.125%	0.1%	156
Al_2O_3/CNF-0.125 %	0.1%	151
CNFs-0.25 %	0.2%	158
Al_2O_3/CNFs-0.25 %	0.2 %	150
CNFs-0.5%	0.4 %	164
Al_2O_3/CNFs-0.5 %	0.4 %	161

3.6 Cement hydration by thermal analysis (TGA)

Derivative thermal analysis (DTA) has been used to determine the corresponding moieties decomposition within the mixture, while thermogravimetric analysis (TGA) determines the mass loss due to the decompositions. The TGA and DTA results for the cement mortar composites for the standard C0, CNFs-0.25 %, and Al_2O_3/CNFs-0.125% were collected at age of 7, 14 and 28 days, respectively, as shown in Figure 3.13. Comparing with C0, the samples with nanomaterials show an increase in the mass loss as presented in Table 3.3. This is an indicator that the addition of the nanomaterial has promoted the degree of hydration (DOH). The DOH contents and calcium hydroxide contents are shown in Figure 3.14. These two measurements metric increase with the age of hydration.

Table 3.3 TGA/DTA analysis of mass losses for specimens C0, CNFs-0.25%, and Al_2O_3/CNFs-0.125%.

Sample	Total mass loss		
	7 days	14 days	28 days
C0	18.6	21.1	22.6
CNFs-0.25%	21.4	22.1	24
Al_2O_3/CNFs-0.125%	21.1	22.4	25

Figure 3.14 (a) displays the degree of hydration as a function of the aging time. The degree of hydration was calculated based on Pane et al. [75]. The latter method determines the degree of hydration by subtracting the mass at 1000ºC from the mass at 140ºC divided by the initial mass. It is seen the DOH increases with aging time. At the age of 7 days there was 7.6% and 2.3% increase in the degree of hydration of CNF-0.25% and Al_2O_3/CNFs-0.125%, respectively. After 14 days, the change was 5.3 % and 3.7% for CNF-0.25% and Al_2O_3/CNFs-0.125%, respectively. However, at 28 days the Al_2O_3/CNFs-0.125% has shown 8% whereas CNFs-0.25% shown 6.1%, respectively. All the data of DOH were reported comparing with C0. This increase in DOH in Al_2O_3/CNFs-0.125% in age of 28 days could be attributed to the hydrophilicity of the Al_2O_3 surface and its ability to adsorb water. The adsorbed water on Al_2O_3/CNFs-0.125% induces the hydration process to produce more C-S-H gel hydration at later age. It may also motivate pozzolanic reaction to produce C-A-H gel by consuming the calcium hydroxide (CH) which is illustrated in Figure 3.14 (b).

One of the important metrics in assessing the extent of the hydration progress is determining the CH content. Figure 3.14 (b) presents the CH content versus the nanomaterial ratios at 7, 14, and 28 days. At age 7 days, the largest amount of CH was

observed in CNFs-0.25% and Al_2O_3/CNFs-0.125% with amount of 17.1 and 16.82%, respectively. By increasing the curing age to 14 days, the CH content in C0 and CNFs-0.25% reach to 17.75% and 18.6% as an indicator that the degree of hydration is increasing with age. However, the CH content in the Al_2O_3/CNFs-0.125% composite was the lowest among the samples. This also could be explained due to the reactivity of the porous layer of alumina that worked to be an effective seeding site for hydration products growth CH and C-S-H. More uniform C-S-H can densify and compact the mortar matric and restrict the growth of the crystal CH. The content of the CH at age of 28 days was also reduced in case of CNFs-composities which can be attributed to the same reason mentioned above. Based on these results, one can conclude that the addition of CNFs increases the degree of hydration also by providing preferential nucleation sites at its oxygen functional groups. The effect of the covalent bonding provided by surface functional groups on CNFs govern its performance [87].

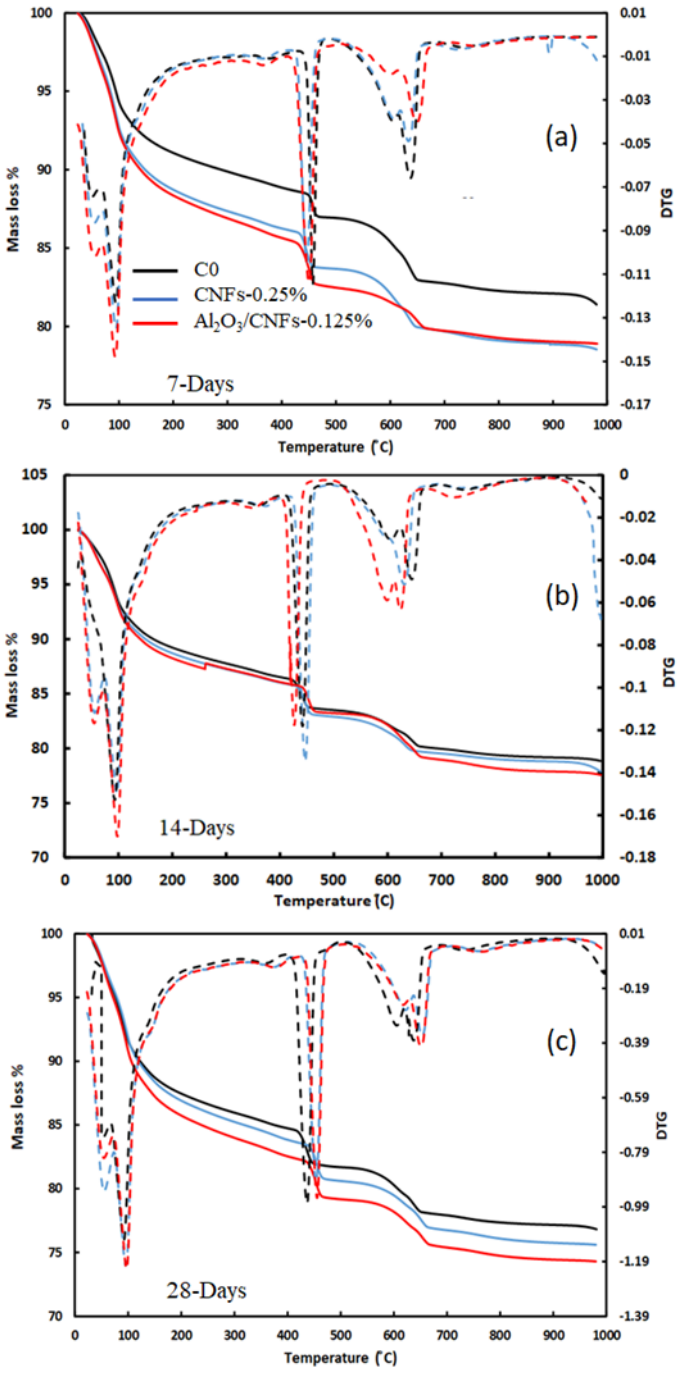

Figure 3.13 TGA analysis for C0, CNFs-0.25%, and Al_2O_3/CNFs-0.125, (a) 7 days, (b) 14 days, (c) 28 days.

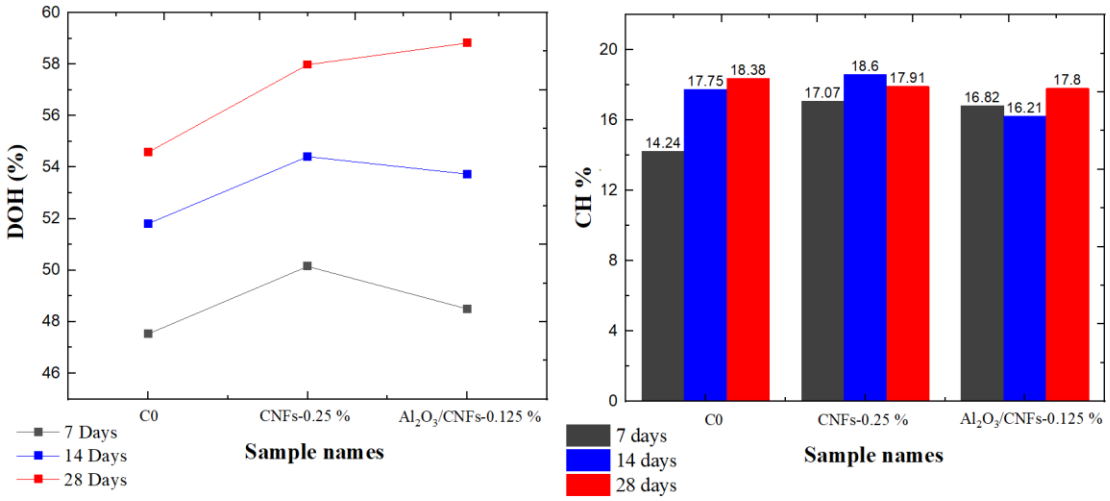

Figure 3.14 TG/DTA analysis of weight losses of C0, CNFs-0.25 % and Al_2O_3/CNFs-0.125 % mortars.

3.7 X-ray diffraction (XRD)

To qualitatively investigate the mineralogical compositions for the mortar composites, the XRD patterns were performed. The results for the samples C0, CNFs-0.25%, and Al_2O_3/CNFs-0.125% at age of 28 days were displayed in Figure 3.15. It is seen that the XRD patterns for all samples show identical diffractions angles. The phases found in all mixtures are ettringite (Aft), portlandite (CH), tricalcium silicate (C_3S), dicalcium silicate (C_2S) and calcium carbonate $CaCO_3$. The diffraction angle of $2\theta = 9.1°$ belongs to ettringite, whereas the peak at $2\theta = 22.5°$ is for $CaCO_3$. The peaks at $2\theta = 18°$, 28°, 47°, 51° and 54° are attributed to calcium hydroxide (CH). The diffraction peaks at $2\theta = 29.5°$, 32°, 34° and 39.3° were assigned to the hydrated C_3S and C_2S [88]. Cement clinker has about 75% chemical components of C_3S and C_2S. These two components react with water to produce crystalline calcium hydroxide or portlandite (CH) and amorphous form of calcium-silicate-hydrate (C-S-H). In addition, these two hydration products comprise over

60% of hydration products. The chemical formulas expressing the hydration reaction of C_3S and C_2S are represented by the equations below [63]:

$C_3S+H_2O\rightarrow$ C-S-H+ CH

$C_2S+H_2O\rightarrow$ C-S-H+ CH

Therefore, paying attention to the peak's intensity of C_2S and C_3S gives a sense on how much C_2S and C_3S already been consumed during the hydration reaction. Figure 3.16 (a and b) show a strong sharp peak of C_3S and C_2S at $2\theta = 29.5°$ in the control sample. The peak intensity decreases when CNFs-0.25% were embedded, and a significant reduction in the peak was observed when Al_2O_3/CNFs-0.125% was in the cement matrix. The results indicate the hydration proceeds more efficiently in Al_2O_3/CNFs followed by CNFs-0.25% and finally C0. Another noted observation from the XRD data is the CH peak at $2\theta = 18°$ as shown in Figure 3. It is observed that the peak has decreased in case of Al_2O_3/CNFs-0.125% relative to other two samples. This indicates the influence on the mortar hydration by accelerating the dissolution of C_3S and C_2S leading to more and better distribution of gel hydration C-S-H. This is also agreeing with EDS analysis by having lower Ca/Si ratio, which means more C-S-H gel hydration was produced in these composites. This growth may restrict the growth of CH as it was observed in the SEM morphology images. Or the less CH intensity may be an indicator of formation of an additional C-A-H gel [49-51, 89]. The hydration gels are amorphous in nature and are not detectable in XRD. Therefore, an indirect measurement can be adapted by focusing on the CH intensity and anhydrate C_3S and C_2S phases. In conclusion, the addition of the CNFs and Al_2O_3/CNFs promoted the

degree of the hydration and this promotion was significant in case of Al_2O_3 presence. These results are in line with the TGA findings described earlier.

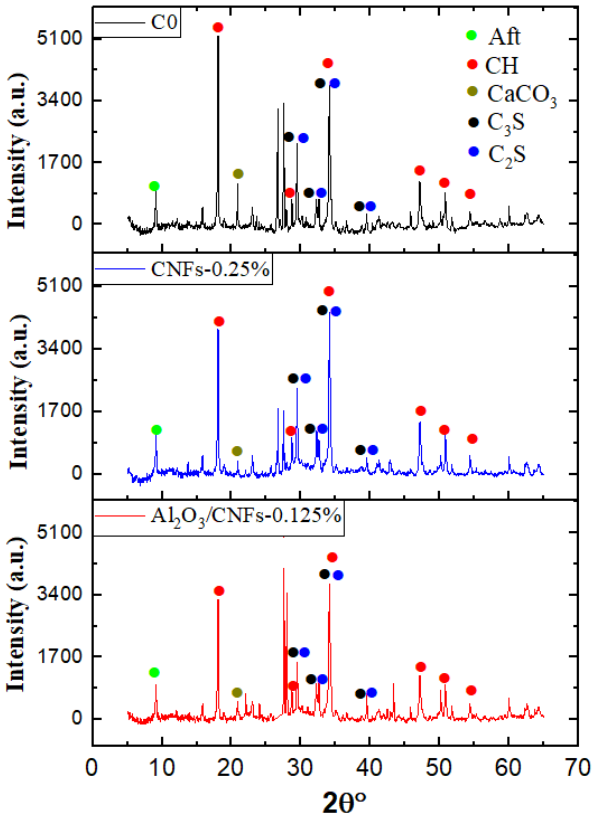

Figure 3.15 XRD patterns total spectrum (a) C0, (b) CNFs-0.25, (c) Al_2O_3/CNFs-0.125%.

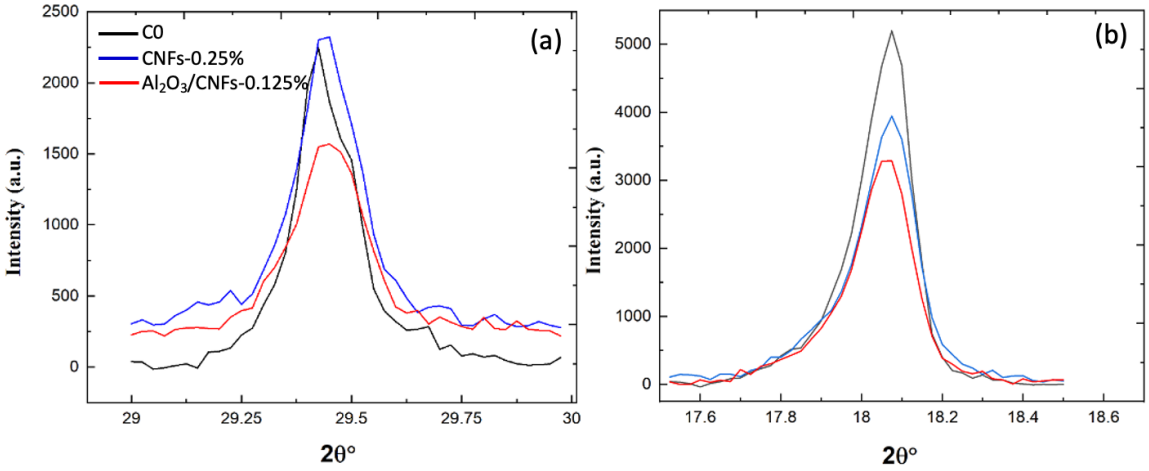

Figure 3.16 Selective peaks (a) C_3S and C_2C peak and (b) CH peak for C0, CNFs-0.25, and Al_2O_3/CNFs-0.125%.

3.8 Freeze-thaw effects

The frost resistance of mortar refers to the capability to withstand the damages caused by the freeze-thaw cycles of water, which is one of the important indices reflecting the durability of cement. To detect the frost resistance of the hardening samples, the mass loss and compressive degradation of samples with optimum dosage of nanomaterials have been calculated as shown in Table 3.3.

3.8.1 Mass loss

In this test, the weight change is monitored during the freezing and thawing cycles. These measurements were conducted after 50, 100, 150, 200, 250 and 300 cycles. As provided in Table 3.4 and shown in Figure 3.17, the mass loss for all mixtures increased with increasing the number of freeze-thaw cycles. By the addition of nanomaterials, the mass loss in the samples was significantly reduced. This illustrates the positive effect of the nanomaterial's addition on the composite's durability. In the case of the control sample, the mass loss was about 8.8% after 300 cycles. While the addition of CNFs at different ratios always lowered mass loss, with the lowest for the case of CNFs-0.25%. This may indicate that the addition of the functionalized CNFs worked to reduce porosity and increase the density of the CNF/cement composites. However, the mass loss has increased when CNFs-0.5 wt.% was embedded in cement mortars. This was expected as these composites shows lower strength due to the large pores that are created in the matrix because of the agglomeration of the CNFs bundles as has been explained earlier in Section 3.4.

Following the same trend, the addition of Al_2O_3/CNFs has shown a remarkable performance in resisting the frost. Overall, the addition of different ratios of Al_2O_3/CNFs

enhanced the frost resistance. The addition of Al_2O_3/CNFs-0.125% and Al_2O_3/CNFs-0.5% show a significant low mass loss after 300 cycles by 1.16% and 1.20%, respectively. This improvement is explained by decreasing the porosity resulting from modifying the internal voids. This might be due to the refinement of the pores structure by producing additional hydrated gels which prevent intrusion of water molecules to the mixture's microstructure. Furthermore, this refinement could be due to the reactivity of the porous Al_2O_3 layer that accelerates the hydration process forming more well distributed C-S-H hydrated gel in the matrix. The less CH crystal and more amorphous C-S-H in Al_2O_3/CNFs-0.125% as shown in SEM/EDS, XRD and TGA/DTA is a testament of this speculation. The small-size voids could minimize the water settling time and subsequently retard the ice volume enlargement. This is expected since a small size void would hold a high internal pressure and surface tension based on physics principles.

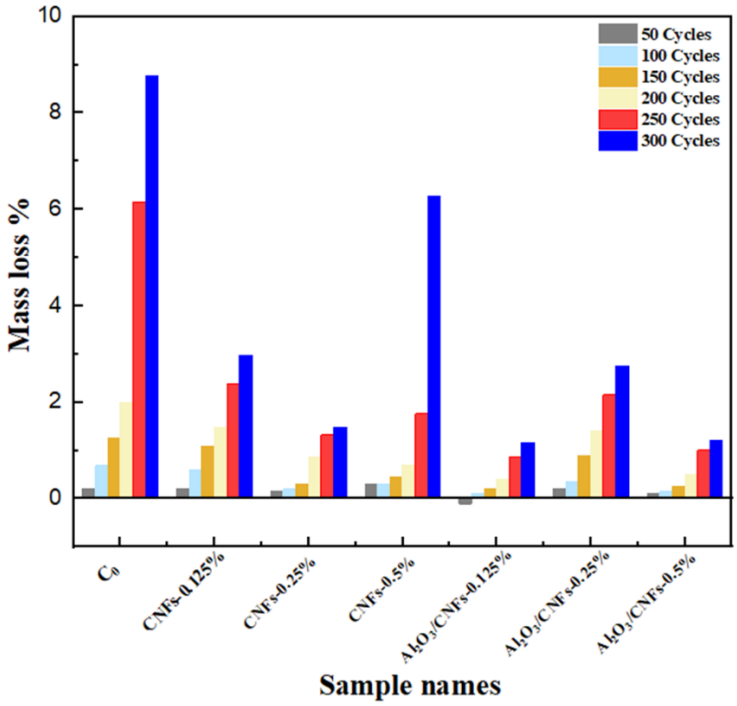

Figure 3.17 Mass loss ratios of mortars samples exposed to freezing-thawing cycles.

Table 3.4 Summary of rapid freezing and thawing results

Mix	Sample number	Weight (lb)						
		Number of Freezing and Thawing Cycles						
		0	50	100	150	200	250	300
C0	1	0.946	0.944	0.94	0.938	0.934	0.9	0.87
	2	0.956	0.954	0.949	0.94	0.93	0.885	0.865
	Average of Mass loss %	0	0.210	0.683	1.259	1.994	6.145	8.776
CNFs-0.125%	1	1.004	1.002	1	0.996	0.994	0.99	0.984
	2	1.01	1.008	1.002	0.996	0.99	0.976	0.97
	Average of Mass loss %	0	0.199	0.595	1.091	1.488	2.380	2.976
CNFs-0.25%	1	0.972	0.971	0.97	0.968	0.965	0.958	0.956
	2	0.992	0.99	0.99	0.99	0.982	0.98	0.979
	Average of Mass loss %	0	0.152	0.204	0.307	0.864	1.325	1.478
CNFs-0.5%	1	1.002	0.998	0.995	0.994	0.992	0.966	0.947
	2	0.99	0.988	0.988	0.984	0.965	0.952	0.92
	Average of Mass loss %	0	0.301	0.450	0.702	1.762	3.716	6.279
Al_2O_3/CNFs-0.125%	1	1.008	1.008	1.007	1.006	1.004	0.998	0.995
	2	0.992	0.994	0.991	0.990	0.988	0.985	0.982
	Average of Mass loss %	0	0.101	0.1	0.2	0.402	0.856	1.16243
Al_2O_3/CNFs-0.25%	1	1.008	1.006	1.005	0.997	0.99	0.984	0.976
	2	0.988	0.986	0.984	0.981	0.978	0.969	0.965
	Average of Mass loss %	0	0.200	0.351	0.899	1.399	2.152	2.751
Al_2O_3/CNFs-0.5%	1	1.002	1.001	1	0.999	0.996	0.990	0.988
	2	0.99	0.989	0.989	0.988	0.986	0.982	0.980
	Average of Mass loss %	0	0.100	0.150	0.2507	0.501	1.003	1.204

3.8.2 Compressive strength post freezing-thawing cycles

Figure 3.18 shows compressive strength versus the number of freeze-thaw cycles at 50, 100, and 150 cycles for C0, CNFs-0.25%, and Al_2O_3/CNFs-0.125% samples. Overall, samples with nanomaterials show less compressive reduction when comparing with C0. Control C0 displayed a decrease of 44.5% in compressive strength after 150 cycles, whereas specimens containing CNFs at ratio of 0.25% showed a decrease of 22%.

Interestingly, the Al_2O_3/CNFs-0.125% has a significant enhancement on mortars frost resistance by showing the least compressive strength reduction of 14%. This performance was confirmed by the Barrett-Joyner-Halenda (BJH) analysis. The BJH indicates the ability of the Al_2O_3/CNFs to further refine the small and medium capillary porous resulting in more compacted and durable composites.

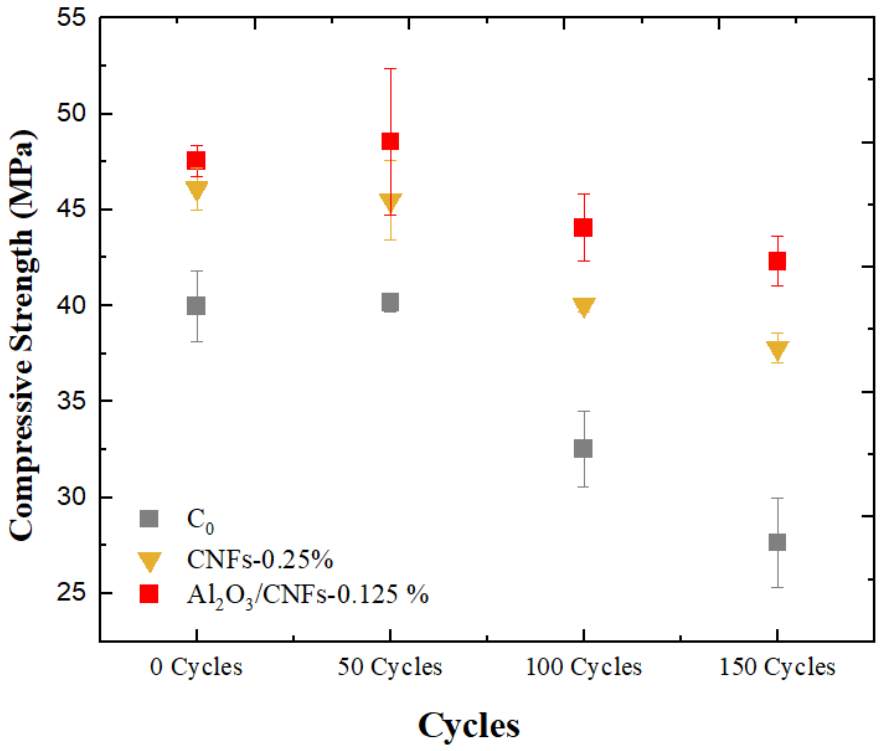

Figure 3.18 Compressive strength for C0, CNFs-0.125% and Al_2O_3 /CNFs-0.125% composites after exposing to freezing-thawing cycles.

Table 3.5 Compressive strength for C0, CNFs-0.25, and Al_2O_3/CNFs 0.125 hardening samples after exposing to freeze-thaw cycles.

Mix	SP %	Compressive strength after 0 cycles		Compressive strength after 50 cycles		Compressive strength after 100 cycles		Compressive strength after 150 cycles	
		Average	S.D.	Average	S.D.	Average	S.D.	Average	S.D.
C0	0	39.97	1.85	40.18	0.51	32.53	1.96	27.66	2.35
CNFs-0.25	0.2	46.11	1.10	45.51	2.06	40.05	0.34	37.82	0.80
Al_2O_3/CNFs-0.125	0.1	48.00	4.96	48.55	3.84	44.05	1.74	42.33	1.32

3.8.3 Physical appearance

The surface of the mortars was observed at regular intervals during the freeze-thaw cycles to record the physical characteristic of the samples. The surface conditions of all samples after 50, 150, and 300 cycles are illustrated in Figures 3.19. After completing 50 cycles, it can be seen from the surface appearance that all samples retained their full shape, and no damage was observed. After 150 cycles as shown in Figure 3.20, the edges of the samples start to deteriorate. A severe impact of freeze-thaw is clearly observed after 300 cycles as shown in Figure 3.21.

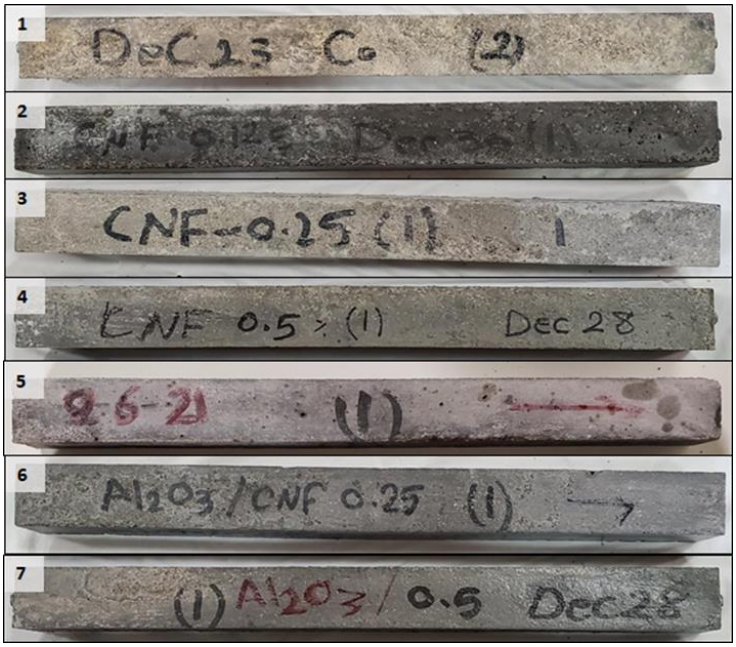

Figure 3.19 Samples after 50 freeze-thaw cycles, (1) C0, (2) CNFs-0.125%, (3) CNFs-0.25%, (4) Al_2O_3/CNFs-0.125%, (5) Al_2O_3/CNFs-0.25%, (6) Al_2O_3/CNFs-0.5%.

Figure 3.19

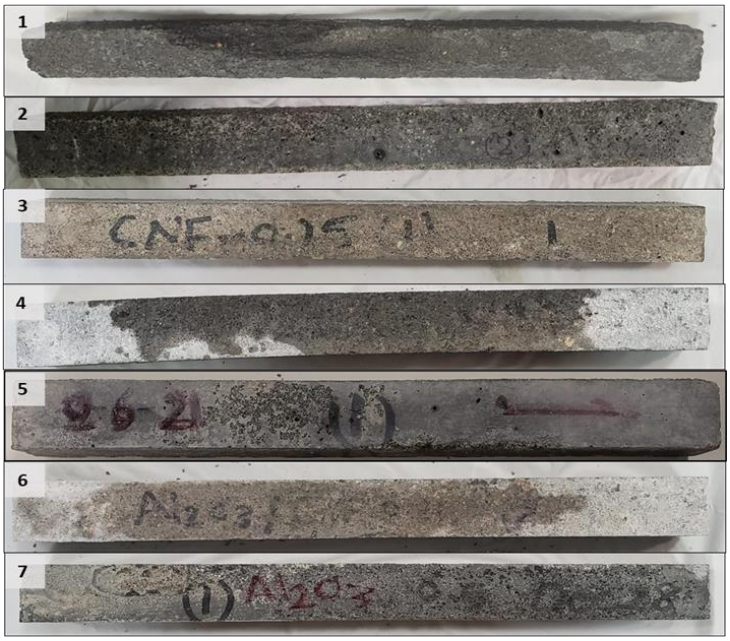

Figure 3.20 Samples after 150 freeze-thaw cycles, (1) C0, (2) CNFs-0.125%, (3) CNFs-0.25%, (4) Al_2O_3/CNFs-0.125%, (5) Al_2O_3/CNFs-0.25%, (6) Al_2O_3/CNFs-0.5%.

The control sample (C0) shows the most surface deformation comparing with the other. At 150 cycles, C0 has experienced partial deteriorations, while after 300 cycles a severe damage was observed. Incorporation of the nanomaterials Al_2O_3/CNFs or CNFs has shown its role by retaining a solid structure of the prism. Particularly, the Al_2O_3/CNFs showed an outstanding performance compared to CNFs. During the freeze-thaw cycling, the cement structure would be vulnerable due to water penetration and phase changing. With the nanomaterials embedded, the structure gets refined which hinders the water degree of freedom to diffuse.

Figure 3.21 Samples after 300 freeze-thaw cycles, (1) C0, (2) CNFs-0.125%, (3) CNFs-0.25%, (4) Al_2O_3/CNFs-0.125%, (5) Al_2O_3/CNFs-0.25%, (6) Al_2O_3/CNFs-0.5%.

3.9 Pore structure results

By using the BET, the surface areas for the samples C0, CNFs-0.25%, Al_2O_3/CNFs-0.125% were calculated and found to be 26.3, 33.8, and 32.6 m^2/g, respectively. The pore volume of the samples was calculated based on the BJH method [90]. The cement mortar powder was grained and filtered by a 300 μm sieve, then it was dried and vacuumed at 200°C for 2 hours during the degassing process. Figure 3.22 (a) shows a type IV isotherm hysteresis for the adsorption-desorption [91]. Figure 3.22 (b) shows the pore volume statistic of the three samples. The pore diameter statistic is divided into four regions. It is seen that the Al_2O_3/CNFs-0.125% has only more volume in a range of (1-10 nm), which are classified as gel pores [92]. The gel pores are related to the formation of C-S-H which is produced by the hydration reaction of the C_3S and C_2S. In other ranges, where the capillary pores presented, the Al_2O_3/CNFs-0.125% pore volume has significantly reduced indicating that the refinement is enhanced. The overall BJH pore volume was also obtained to be 0.07805, 0.06783, and 0.06278 ml/g for C0, CNFs-0.25%, and Al_2O_3/CNFs-0.125%, respectively. The pore refinement is also induced when the CNFs was incorporated, however, the Al_2O_3/CNFs-0.125% has further reduced the pore volume which is maybe due to the higher C-S-H content as was described in previous characterizations (Sections 3.5 and 3.2.2.2). It may also be due to pozzolanic reaction offered by the Al_2O_3 nanocoating which helps producing extra C-A-H. Most recently, a study has demonstrated the effect of different aluminum oxide phases ($Al(OH)_3$, γ-Al_2O_3, α-Al_2O_3) on the calcium aluminate cement hydration [93]. In another study, it was found that $Al(OH)_3$ significantly accelerates the hydration due to the high surface area and the ability to serve as a nucleation center for

C-A-H moiety [94]. This is in line with the results obtained in this study as the aluminum oxide is in boehmite phase as confirmed by the XRD as shown in this reference [67].

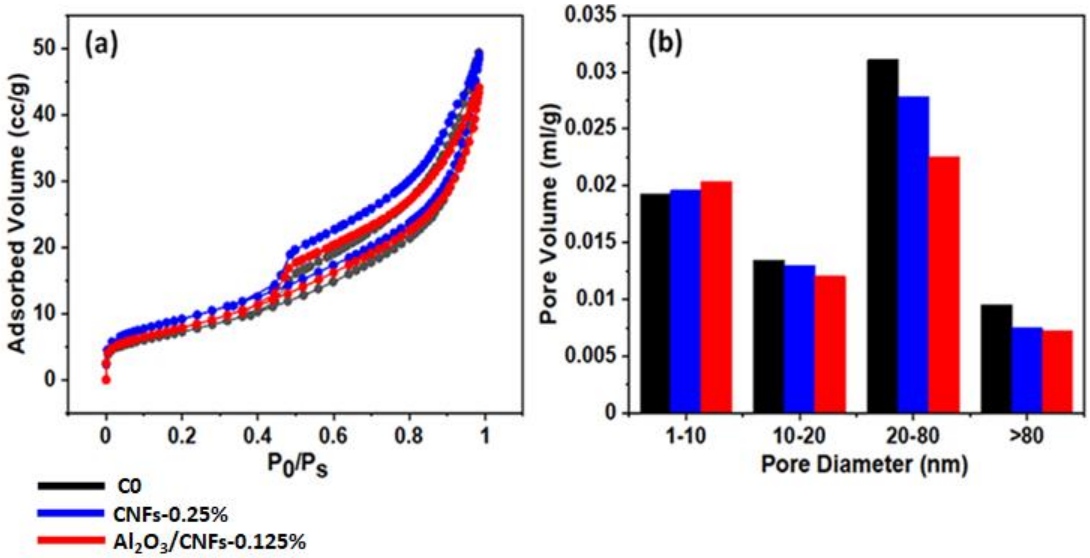

Figure 3.22 (a) BET isotherm analysis, (b) Pore volume distribution.

3.10 Drying shrinkage results

The effect of the addition of the nanomaterials on the drying shrinkage was studied as in Figure 3.23. and Table 3.6 at a water/cement ratio of 40%. Additional information is provided in the Appendix. The results indicate that the cement mortars with CNFs and Al_2O_3-coated CNFs have lower shrinkage compared to C0 mortar at early and late ages. In comparison with C0, the average early drying shrinkage of composites that was reinforced by CNFs at ratios of 0.125%, 0.25% and 0.5% showed noticeable decrease by about 19%, 33% and 22%, respectively at age of 7 days. While, after 56 days, the reduction was about 16%, 20% and 14%. In addition, the results of Table 3.6 show remarkable reduction in the drying shrinkage for the composites that contains Al_2O_3/CNFs at various ratios. It is clearly that the addition of the Al_2O_3/CNFs-0.125% has significantly reduced the shrinkage

relative to other samples, whether in the early or late age. At age of 7 days and 56 days, the Al_2O_3/CNFs-0.125% has reduced the shrinkage by 62% and 47% compared to the standard (C0), respectively at the same comparison, the Al_2O_3/CNFs-0.25% has shown 36% and 27% shrinkage reduction at the same time periods. On the other hand, the composites that contains 0.5% of Al_2O_3/CNFs exhibited low shrinkage by 30% and 17% at age 7 and 56, respectively.

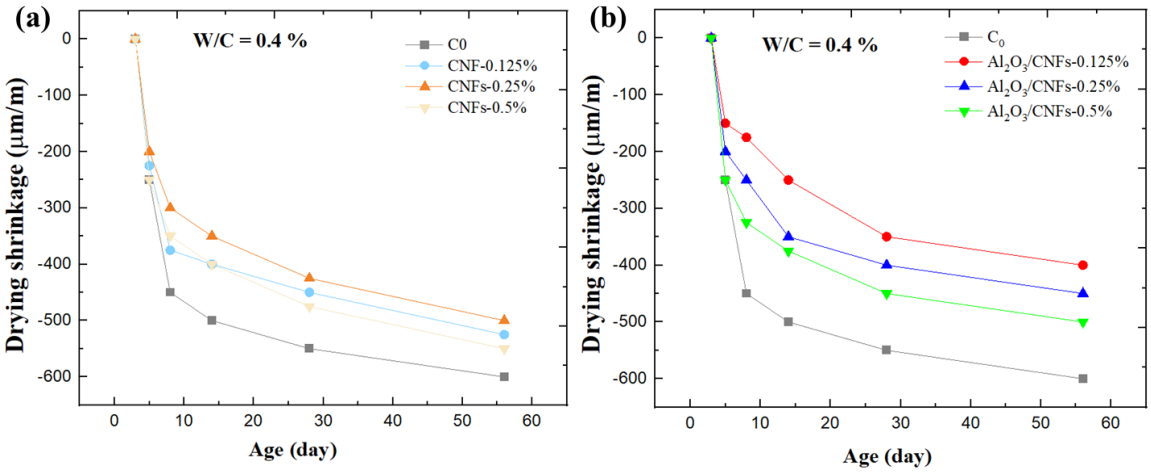

Figure 3.23 (a) Drying shrinkage of the CNFs composites at different ratios in comparison with control sample at different ages. (b) Drying shrinkage of the Al_2O_3/CNFs composites at different ratios with comparison to control sample at different ages.

Table 3.6 Average drying shrinkage results for C0, CNFs-composites, and Al_2O_3/CNFs-composites at different curing ages

Mix	Sample number	Average Shrinkage (um)					
		Age 3 days	Age 5 days	Age 7 days	Age 14 days	Age 28 days	Age 56 days
C0	**1**	0	-210	-420	-550	-610	-670
	2	0	-290	-510	-490	-560	-600
	Average	0	-250	-465	-520	-585	-635
CNFs-0.125%	1	0	-330	-420	-450	-470	-580
	2	0	-120	-330	-360	-420	-490
	Average	0	-225	-375	-405	-445	-535
CNFs-0.25%	1	0	-80	-220	-280	-330	-420
	2	0	-310	-400	-450	-510	-600
	Average	0	-195	-310	-365	-420	-510
CNFs-0.5%	1	0	-290	-500	-560	-600	-660
	2	0	-190	-220	-280	-340	-430
	Average	0	-240	-360	-420	-470	-545
Al_2O_3/CNFs-0.125%	1	0	-170	-200	-280	-320	-370
	2	0	-100	-150	-240	-390	-440
	Average	0	-135	-175	-260	-355	-405
Al_2O_3/CNFs-0.25%	1	0	-150	-270	-360	-460	-540
	2	0	-340	-380	-410	-460	-510
	Average	0	-245	-325	-385	-460	-525
Al_2O_3/CNFs-0.5%	1	0	-210	-230	-300	-350	-450
	2	0	-220	-260	-360	-450	-480
	Average	0	-215	-245	-330	-400	-465

Drying shrinkage of cementitious materials is due to capillary surface tension because of the meniscus formation in the capillary pores. As it was discussed previously in BET/BJH measurement (Section 3.7), the incorporation of both CNFs and Al_2O_3/CNFs to the mortar matrix reduced the total overall porosity. Besides, increasing the stiffness due to the micro

crack bridging effect of these nanomaterials, it can be effective to reduce the shrinkage deformation. Furthermore, the Al_2O_3 porous layer worked as a reactive site to increase the nucleation that worked to densify and to compact the microstructure of the matrix. The refinement in capillary pores served as an obstacle impeding for the water loss from the cement skeleton [95, 96]. The mitigation of the drying shrinkage for the Al_2O_3/CNFs composites can be due to the high hydrophilicity of these nanomaterials. The Al_2O_3 nanocoating is in a boehmite phase [67], which has a strong ability to absorb and retain water as long as it is in equilibrium with surrounding cement compounds. When the shrinkage takes place, the water is released for the gel to achieve the internal hydration equilibrium [97].

Chapter Four: Conclusion and Recommendations

4.1 General

The use of nanotechnology in reinforcing cementitious composites has gained much attention. Due to their favorable mechanical and chemical properties, nanomaterials have become a promising option for engineering applications in construction and building materials. Moreover, there has been intensive research efforts to enhance the mechanical and durability properties of cementitious composites using variety types of nanomaterials such as, carbon nanomaterials, metal oxides nanomaterials, and hybrid nanomaterials. In this thesis an efficient combination between metal oxides and carbon nanomaterials was achieved. The hybrid effect of the alumina nanocoating of carbon nanofibers enhanced the strength of cementitious composites through two main mechanisms. Porous layer of alumina coating increased the bonding of the CNF to the cementitious matrix and the CNFs bridged the nanocrack areas. Both mechanisms also reduced the permeability of the cementitious composites leading to an improved durability performance.

4.2 Conclusions

Selectively designed nanomaterials were used to embed in cementitious composites. Carbon nanofibers coated with aluminum oxide nanocoating were used in this research. Three sets of samples were prepared with different mass ratios of 0.125, 0.25, and 0.5 wt.% of the cement mass of bare CNFs and Al_2O_3/CNFs. The results of this thesis demonstrated that Al_2O_3/CNFs enhanced the response of cement mortars to destructive environmental

impact, such as freezing and thawing. Also, the inclusion of optimum dosage of Al_2O_3/CNFs in cementitious composites mitigated the drying shrinkage issue.

The TEM images revealed that a well-coated layer was present on the CNF surfaces. The SEM results have shown that the nanomaterials were well-distributed in the microstructure. The SEM images indicate the formation of the hydration products gels such as CH, C-S-H, and ettringite. In case of Al_2O_3/CNFs-mortar composite, most of the hydrated products were well-distributed C-S-H as they were identified from their amorphous appearance, while CNFs-mortar composites have shown mostly ettringite and hexagonal CH. Usually these two types of hydration products do not have significant effect on the strength of the cement composites. In addition, SEM revealed a visual evidence on ability of Al_2O_3/CNFs to bridge micro cracks. The EDS elementals mapping, and its spectrum revealed additional information; the spectrum displays the Ca/ Si ratio as a metric to assess the hydration reaction process. The Ca/Si of Al_2O_3/CNFs-0.125% has shown 3.59 ratio of Ca/Si, however, CNFs-0.25 and C0 have shown a ratio of 4.02, and 10.97.

From the compressive strength tests, the results showed that with increasing the curing age all samples experienced an increasing in their strength. The compressive strength for samples that contain of CNFs- 0.125, 0.25 and 0.5 % wt. of cement increased by 15%, 36% and 23% at age of 7 days. At age of 14 days, the compressive strength of these composites increased by 8%, 23.5% and 14%, respectively. With increasing the curing age of these samples at age 28 days, the improvement of the compressive strength was 5.5%, 15% and 3%, respectively. The composites that contain the Al_2O_3/CNFs have shown progressive improvements compared to others evaluated in this research. Relative to control specimens,

the addition of the Al_2O_3/CNFs-0.125 wt.% increased the strength by 35.6%, 27% and 19% at age 7, 14 and 28 days, respectively.

Superplasticizer was effective to offset the reduction in fluidity of composites due to addition of nanomaterials. Overall, all mixtures showed higher fluidity compared to control samples. However, mixtures that contain Al_2O_3/CNFs with different ratios show a lower fluidity compared to CNFs mixtures. This observation is due to high-hydrophilic surface area of Al_2O_3/CNFs nanomaterials that absorbed more water to get their surface wet.

TGA/DTA testes showed that all CNFs and Al_2O_3/CNF composites exhibited higher degrees of hydration than the control samples. Increasing calcium hydroxide is an indicator that samples have more hydration products. However, this was not the case for samples that contains Al_2O_3/CNFs at age 14 and 28 days and for sample that contain CNFs at age 28 days. This could be due to the nucleation effect which produced a well-distribution of the gel hydration C-S-H inside the mortar matrix that restricts the growth of the CH. Also, this may be due to the pozzolanic effect of the Al_2O_3 layer. At the presence of water, the Al_2O_3 can participate in producing the secondary gels C-A-H, and therefore more CH was consumed. To further confirm the data, XRD pattern for the optimum samples at age 28 days were conducted. The XRD measurement focused on the intensity of two cementitious moieties, first the C_2S and C_3S as the to be consumed in the hydration reaction. Al_2O_3/CNFs-0.125% has shown the lowest intensity of these two compounds, which indicates that they increased the dissolution of C_3S and C_2S, and thus more C-S-H was produced. In addition, XRD data focused on the intensity of CH as it has shown lower intensity in case of CNFs-0.25% and Al_2O_3/CNFs 0.125% composites. These results are in good agreement with TGA and EDS analyses findings.

The addition of Al_2O_3/CNFs-0.125% and Al_2O_3/CNFs-0.5% showed a significant low mass loss after 300 freeze-thaw cycles by 1.16% and 1.2%, respectively. Whereas the reference sample and CNFs-0.25 have shown a mass loss of 8.8 and 2.75%, respectively.

In case of the compressive strength degradation, samples with Al_2O_3/CNFs-0.125% showed lower degradation with about 14% after 150 freeze-thaw cycles. Control specimens displayed a decrease of 44.5% in compressive strength after 150 cycles, whereas specimens containing CNFs at ratio of 0.25% showed a decrease of 22%. From the physical appearance, the Al_2O_3/CNFs-0.125 % and Al_2O_3/CNFs-0.5% were superior relative to the other samples with a minimal destruction. Those results were assigned to the highly dense microstructure which was later confirmed by the BET measurements. The BET and BJH tests have exhibited low gas adsorption and more refinement in the capillary pores.

The results indicate that the cement mortars with CNFs and Al_2O_3-coated CNFs have low drying shrinkage compared to control mortar at early and late ages. In comparison with control mortar, the average early drying shrinkage of composites that were reinforced by CNFs at ratios of 0.25 % showed noticeable decrease by about 33% and 20% at age of 7, and 56 days, respectively. Overall, the performance of samples with Al_2O_3/CNFs was superior to other cement composites evaluated, which is attributed to their high hydrophilicity.

4.3 Recommendations

To advance the research presented in this thesis, additional work is needed to develop a better understanding of various parameters of nanomaterials and coatings and their effect

on the mechanical and durability performance of cementitious composites. A summary of some of these recommendations for future research is listed below:

- Study the effect of the superplasticizer on the Al_2O_3 coating layer and the composite fluidity.
- Detailed durability investigation of cement composites that contain alumina-coated carbon nanofibers.
- Study the effect of the alumina-coated carbon nanofibers on drying shrinkage with different water-to-cement ratios, various temperatures, relative humidity, and volumetric size.
- Perform SEM-EDS characterizations on smaller specimens. This is expected to improve the accuracy and reduce the uncertainty in the nanomaterials' distribution in the cement mortar.
- Perform additional investigations using a lower and wider range of nanomaterials weight loading, such 0.0625 – 0.20 wt.%.
- Study large capillary pores using other indirect methods, such as water absorption and mercury intrusion porosimeter.
- Study other metal oxides coating layers, such as SiO_2, which offers a superior level of pozzolanic activity.
- Study other substrate to coat from carbon nanomaterials family, such as carbon black, which is a byproduct of tires production. This combination could offer a cost-effective use of waste materials for a nanotechnology application in construction and building materials.

BIBLIOGRAPHY

[1] P.N. Balaguru, S.P. Shah, Fiber-reinforced cement composites, 1992.

[2] A. Bentur, S. Mindess, Fibre reinforced cementitious composites, Crc Press2006.

[3] H.A. Kottb, N.F. El-Shafey, A.A. Torkey, Behavior of high strength concrete columns under eccentric loads, HBRC Journal, 11 (2015) 22-34.

[4] Y. Fan, S. Zhang, Q. Wang, S.P. Shah, Effects of nano-kaolinite clay on the freeze–thaw resistance of concrete, Cem. Concr. Compos., 62 (2015) 1-12.

[5] T.C. Powers, A working hypothesis for further studies of frost resistance of concrete, Journal Proceedings, 1945, pp. 245-272.

[6] V. Penttala, Freezing-induced strains and pressures in wet porous materials and especially in concrete mortars, Advanced cement based materials, 7 (1998) 8-19.

[7] P. Monteiro, Concrete: microstructure, properties, and materials, McGraw-Hill Publishing2006.

[8] T.C. Powers, T. Willis, The air requirement of frost resistant concrete, Highway Research Board Proceedings, 1950.

[9] T.C. Powers, R. Helmuth, Theory of volume changes in hardened portland-cement paste during freezing, Highway research board proceedings, 1953.

[10] T. Zhou, K. Ioannidou, F.-J. Ulm, M.Z. Bazant, R.-M. Pellenq, Multiscale poromechanics of wet cement paste, Proc. Natl. Acad. Sci. U.S.A., 116 (2019) 10652-10657.

[11] A. Neville, Properties of concrete 3rd edition, J Pitman, London, (1981).

[12] E. Freyssinet, Théorie générale de la prise des liants hydrauliques; les phénomènes de retrait et de déformation lente des bétons et mortiers, %J CR Centre d'Etudes Supérieures de l'Inst. Techn. Bâtiment Trav. Publ., Paris, (1934) 321.

[13] T.C. Powers, Mechanism of shrinkage and reversible creep of hardened cement paste, Proc. Int. Symp. Concr., London, 1965, 1965.

[14] R. Feldman, P. Sereda, A new model for hydrated Portland cement and its practical implications, Engineering Journal, 53 (1970) 53-59.

[15] F. Wittmann, Surface tension skrinkage and strength of hardened cement paste, Matériaux et Construction, 1 (1968) 547-552.

[16] I. Soroka, Portland cement paste and concrete, Macmillan International Higher Education1979.

[17] Z.P. Bazant, F.H. Wittmann, Creep and shrinkage in concrete structures, (1982).

[18] M. del Carmen Camacho, O. Galao, F.J. Baeza, E. Zornoza, P. Garcés, Mechanical properties and durability of CNT cement composites, Materials & Design, 7 (2014) 1640-1651.

[19] C. Camacho-Ballesta, Ó. Galao, F.J. Baeza, E. Zornoza, P. Garcés, Durability and Mechanical Properties of CNT Cement Composites, Springer International Publishing, Cham, 2019, pp. 31-41.

[20] D. Nivethitha, S. Srividhya, S. Dharmar, Review on mechanical properties of cement mortar enhanced with nanoparticles, International Journal of Science Research and Development News/R & D News, 5 (2016) 913-916.

[21] S. Chuah, Z. Pan, J.G. Sanjayan, C.M. Wang, W.H.J.C. Duan, B. Materials, Nano reinforced cement and concrete composites and new perspective from graphene oxide, 73 (2014) 113-124.

[22] K. Ebrahimi, M.J. Daiezadeh, M. Zakertabrizi, F. Zahmatkesh, A.H.J.C. Korayem, B. Materials, A review of the impact of micro-and nanoparticles on freeze-thaw durability of hardened concrete: Mechanism perspective, 186 (2018) 1105-1113.

[23] S. Kumar, P. Kolay, S. Malla, S. Mishra, Effect of Multiwalled Carbon Nanotube in Cement Composite on Mechanical Strength and Freeze-Thaw Susceptibility, Advances in Civil Engineering Materials, 4 (2015) 257-274.

[24] A. Mohammed, J. Sanjayan, W. Duan, A. Nazari, Graphene oxide impact on hardened cement expressed in enhanced freeze–thaw resistance, J. Mater. Civ. Eng., 28 (2016) 04016072.

[25] S. Vardharajula, S.Z. Ali, P.M. Tiwari, E. Eroğlu, K. Vig, V.A. Dennis, S.R. Singh, Functionalized carbon nanotubes: biomedical applications, International journal of nanomedicine, 7 (2012) 5361.

[26] A.M. Jasim, S.E. Hoff, Y. Xing, Enhancing methanol electrooxidation activity using double oxide catalyst support of tin oxide clusters on doped titanium dioxides, Electrochim. Acta, 261 (2018) 221-226.

[27] J.-P. Salvetat, J.-M. Bonard, N. Thomson, A. Kulik, L. Forro, W. Benoit, L. Zuppiroli, Mechanical properties of carbon nanotubes, Appl. Phys. A, 69 (1999) 255-260.

[28] I. Kang, Y.Y. Heung, J.H. Kim, J.W. Lee, R. Gollapudi, S. Subramaniam, S. Narasimhadevara, D. Hurd, G.R. Kirikera, V. Shanov, Introduction to carbon nanotube and nanofiber smart materials, Composites Part B: Engineering, 37 (2006) 382-394.

[29] A.K. Geim, K.S. Novoselov, The rise of graphene, Nanoscience and technology: a collection of reviews from nature journals, World Scientific2010, pp. 11-19.

[30] A. Ashour, Aspect Ratio Effect of Functionalized/Non-Functionalized Multiwalled Carbon Nanotubes on the Mechanical Properties of Cementitious Materials, Texas A & M University, 2012.

[31] M. Brahmayya, S.A. Dai, S.-Y. Suen, Sulfonated reduced graphene oxide catalyzed cyclization of hydrazides and carbon dioxide to 1, 3, 4-oxadiazoles under sonication, Scientific Reports, 7 1-13.

[32] H. Lee, S. Jeong, S. Cho, W. Chung, Enhanced bonding behavior of multi-walled carbon nanotube cement composites and reinforcing bars, Composite Structures, 243 (2020) 112201.

[33] R.K. Abu Al-Rub, A.I. Ashour, B.M. Tyson, On the aspect ratio effect of multi-walled carbon nanotube reinforcements on the mechanical properties of cementitious nanocomposites, Construction and Building Materials, 35 (2012) 647-655.

[34] W.-W. Li, W.-M. Ji, Y.-C. Wang, Y. Liu, R.-X. Shen, F. Xing, Investigation on the mechanical properties of a cement-based material containing carbon nanotube under drying and freeze-thaw conditions, J Materials, 8 (2015) 8780-8792.

[35] A. Cwirzen, K. Habermehl-Cwirzen, The effect of carbon nano-and microfibers on strength and residual cumulative strain of mortars subjected to freeze-thaw cycles, Journal of Advanced Concrete Technology, 11 (2013) 80-88.

[36] T. Wang, J. Xu, B. Meng, G. Peng, Experimental study on the effect of carbon nanofiber content on the durability of concrete, Construction and Building Materials, 250 (2020) 118891.

[37] Z.S. Metaxa, M.S. Konsta-Gdoutos, S.P. Shah, Carbon nanofiber–reinforced cement-based materials, Transportation Research Record, 2142 (2010) 114-118.

[38] T. Shi, Z. Li, J. Guo, H. Gong, C. Gu, Research progress on CNTs/CNFs-modified cement-based composites–a review, Construction and Building Materials, 202 (2019) 290-307.

[39] A. Peigney, C. Laurent, E. Flahaut, R. Bacsa, A. Rousset, Specific surface area of carbon nanotubes and bundles of carbon nanotubes, Carbon, 39 (2001) 507-514.

[40] A. Fehervari, A.J.N. MacLeod, E.O. Garcez, L. Aldridge, W.P. Gates, Y. Yang, F. Collins, On the mechanisms for improved strengths of carbon nanofiber-enriched mortars, Cement Concrete Research, 136 (2020) 106178.

[41] S. Wang, J.L.G. Lim, K.H. Tan, Performance of lightweight cementitious composite incorporating carbon nanofibers, Cement Concrete Composites, 109 (2020) 103561.

[42] X. Fu, W. Lu, D. Chung, Ozone treatment of carbon fiber for reinforcing cement, Carbon, 36 (1998) 1337-1345.

[43] A. Hawreen, J. Bogas, Creep, shrinkage and mechanical properties of concrete reinforced with different types of carbon nanotubes, Construction Building Materials, 198 (2019) 70-81.

[44] S.-J. Lee, S. Kawashima, K.-J. Kim, S.-K. Woo, J.-P. Won, Shrinkage characteristics and strength recovery of nanomaterials-cement composites, Compos. Struct., 202 (2018) 559-565.

[45] M.S. Chavali, M.P. Nikolova, Metal oxide nanoparticles and their applications in nanotechnology, SN Applied Sciences, 1 (2019) 1-30.

[46] J. Mei, T. Liao, L. Kou, Z. Sun, Two-dimensional metal oxide nanomaterials for next-generation rechargeable batteries, Advanced Materials, 29 (2017) 1700176.

[47] A.N. Givi, S.A. Rashid, F.N.A. Aziz, M.A.M. Salleh, Experimental investigation of the size effects of SiO2 nano-particles on the mechanical properties of binary blended concrete, Composites Part B: Engineering, 41 (2010) 673-677.

[48] Y.J.C. Reches, B. Materials, Nanoparticles as concrete additives: Review and perspectives, 175 (2018) 483-495.

[49] K. Behfarnia, N. Salemi, The effects of nano-silica and nano-alumina on frost resistance of normal concrete, Construction and Building Materials, 48 (2013) 580-584.

[50] S. El-Gamal, S. Abo-El-Enein, F. El-Hosiny, M. Amin, M. Ramadan, Thermal resistance, microstructure and mechanical properties of type I Portland cement pastes containing low-cost nanoparticles, Journal of Thermal Analysis Calorimetry, 131 (2018) 949-968.

[51] A. Nazari, S. Riahi, S. Riahi, S.F. Shamekhi, A. Khademno, Influence of Al_2O_3 nanoparticles on the compressive strength and workability of blended concrete, Journal of American Science, 6 (2010) 6-9.

[52] K. Behfarnia, N.J.C. Salemi, B. Materials, The effects of nano-silica and nano-alumina on frost resistance of normal concrete, 48 (2013) 580-584.

[53] R. Zhang, X. Cheng, P. Hou, Z. Ye, Influences of nano-TiO2 on the properties of cement-based materials: Hydration and drying shrinkage, Construction Building Materials, 81 (2015) 35-41.

[54] J. Wang, Y. Cheng, L. Yuan, D. Xu, P. Du, P. Hou, Z. Zhou, X. Cheng, S. Liu, Y. Wang, Effect of nano-silica on chemical and volume shrinkage of cement-based composites, Construction Building Materials, 247 (2020) 118529.

[55] H.A. Abdel-Gawwad, M.S. Mohammed, T. Alomayri, Single and dual effects of magnesia and alumina nano-particles on strength and drying shrinkage of alkali activated slag, Construction Building Materials, 228 (2019) 116827.

[56] F. Sanchez, C. Ince, Microstructure and macroscopic properties of hybrid carbon nanofiber/silica fume cement composites, Composites Science Technology and Health Care, 69 (2009) 1310-1318.

[57] A. Yazdanbakhsh, Z. Grasley, Utilization of silica fume to stabilize the dispersion of carbon nanofilaments in cement paste, J. Mater. Civ. Eng., 26 (2014) 06014010.

[58] P. Stynoski, P. Mondal, C. Marsh, Effects of silica additives on fracture properties of carbon nanotube and carbon fiber reinforced Portland cement mortar, Cem. Concr. Compos., 55 (2015) 232-240.

[59] P. Sikora, M.A. Elrahman, S.-Y. Chung, K. Cendrowski, E. Mijowska, D. Stephan, Mechanical and microstructural properties of cement pastes containing carbon nanotubes and carbon nanotube-silica core-shell structures, exposed to elevated temperature, Cem. Concr. Compos., 95 (2019) 193-204.

[60] M. Garg, C.S. Das, Use of silica particles to improve dispersion of-COOH CNTs/carbon fibers to produce HyFRCC, Construction and Building Materials, 250 (2020) 118777.

[61] H. Kim, I.W. Nam, H.-K. Lee, Enhanced effect of carbon nanotube on mechanical and electrical properties of cement composites by incorporation of silica fume, Compos. Struct., 107 (2014) 60-69.

[62] L. Zhang, L. Li, Y. Wang, X. Yu, B. Han, Multifunctional cement-based materials modified with electrostatic self-assembled CNT/TiO2 composite filler, Construction Building Materials, 238 (2020) 117787.

[63] G. Gurumurthy, A. Hunashya, S. Quadri, N. Banapurmath, A.S. Shetter, R.K. Hiremath, S.A. Hallad, Effect of Multiwalled Carbon Nanotubes and Nano Aluminum Oxide On Flexural and Compressive Strength of Cement Composites, International Journal of Advance Research In Science Engineering and Mining Journal, 3 (2014) 215-223.

[64] J. Makar, J. Margeson, J. Luh, Carbon nanotube/cement composites-early results and potential applications, Proceedings of the 3rd international conference on construction materials: performance, innovations and structural implications, Vancouver Canada, 2005, pp. 1-10.

[65] C. Song, G. Hong, S. Choi, Effect of dispersibility of carbon nanotubes by silica fume on material properties of cement mortars: Hydration, pore structure, mechanical properties, self-desiccation, and autogenous shrinkage, Construction Building Materials, 265 (2020) 120318.

[66] S. Dong, D. Wang, A. Ashour, B. Han, J. Ou, Nickel plated carbon nanotubes reinforcing concrete composites: from nano/micro structures to macro mechanical properties, Composites Part A: Applied Science and Manufacturing, 141 (2021) 106228.

[67] A.M. Jasim, X. He, T.A. White, Y. Xing, Nano-layer deposition of metal oxides via a condensed water film, Communications Materials, 1 (2020) 9.

[68] A. Jasim, X. He, T. White, Y. Xing, Crystallization of Amorphous Alumina Whiskers on Carbon Nanotubes Under Electron Beam Irradiation, Microsc. Microanal., 25 (2019) 1988-1989.

[69] P.-C. Ma, N.A. Siddiqui, G. Marom, J.-K. Kim, Dispersion and functionalization of carbon nanotubes for polymer-based nanocomposites: a review, Composites Part A: Applied Science Manufacturing, 41 (2010) 1345-1367.

[70] N.B. Winter, N.B. Winter, Scanning electron microscopy of cement and concrete, WHD Microanalysis2012.

[71] T. Nochaiya, A.J.A.S.S. Chaipanich, Behavior of multi-walled carbon nanotubes on the porosity and microstructure of cement-based materials, 257 (2011) 1941-1945.

[72] H.-A. Nguyen, T.-P. Chang, J.-Y. Shih, C.-T. Chen, Influence of low calcium fly ash on compressive strength and hydration product of low energy super sulfated cement paste, Cem. Concr. Compos., 99 (2019) 40-48.

[73] W. Deboucha, N. Leklou, A. Khelidj, M.N.J.C. Oudjit, B. Materials, Hydration development of mineral additives blended cement using thermogravimetric analysis (TGA): Methodology of calculating the degree of hydration, 146 (2017) 687-701.

[74] T. Kim, J. Olek, Effects of sample preparation and interpretation of thermogravimetric curves on calcium hydroxide in hydrated pastes and mortars, Transportation Research Record, 2290 (2012) 10-18.

[75] I. Pane, W. Hansen, Investigation of blended cement hydration by isothermal calorimetry and thermal analysis, Cement Concrete Research, 35 (2005) 1155-1164.

[76] A.J.A.I. Standard, West Conshohocken, PA, ASTM C109 / C109M-standard test method for compressive strength of hydraulic cement mortars (using 2-in. or [50 mm] cube specimens), (20b).

[77] A.J.S.T.M.f.F.o.H.C.M.A. Standard, West Conshohocken, PA, C1437-13, (2013).

[78] Standard test method for resistance of concrete to rapid freezing and thawing, ASTM International Committee C09 on Concrete and Concrete Aggregates2008.

[79] C.J.A.I. Astm, West Conshohocken, 490.(2011). Standard Practice for Use of Apparatus for the Determination of Length Change of Hardened Cement Paste, Mortar, and Concrete, 1-5.

[80] A. C596-18, Standard Test Method for Drying Shrinkage of Mortar Containing Hydraulic Cement, ASTM International, (2018).

[81] S. Sharma, N. Kothiyal, Comparative effects of pristine and ball-milled graphene oxide on physico-chemical characteristics of cement mortar nanocomposites, Construction Building Materials, 115 (2016) 256-268.

[82] D.d. Silva Andrade, J.H.d. Silva Rêgo, P.C. Morais, A.N.d. Mendonça Lopes, M. Frías, Investigation of CSH in ternary cement pastes containing nanosilica and highly-reactive supplementary cementitious materials (SCMs): Microstructure and strength, (2019).

[83] A. Peyvandi, P. Soroushian, N. Abdol, A.M. Balachandra, Surface-modified graphite nanomaterials for improved reinforcement efficiency in cementitious paste, Carbon, 63 (2013) 175-186.

[84] T. Shi, Z. Li, J. Guo, H. Gong, C. Gu, Research progress on CNTs/CNFs-modified cement-based composites–a review, Construction Building Materials, 202 (2019) 290-307.

[85] A. Najigivi, A. Khaloo, Iraji zad A and Abdul Rashid S 2013 Investigating the effects of using different types of SiO 2 nanoparticles on the mechanical properties of binary blended concrete J, Compos. Eng., 52-58.

[86] S. Paul, A. van Rooyen, G. van Zijl, L. Petrik, A review of nanoparticles in cement-based materials, Constr Build Mater, 189 (2018) 1019-1034.

[87] J.M. Makar, G.W. Chan, Growth of cement hydration products on single-walled carbon nanotubes, J. Am. Ceram. Soc., 92 (2009) 1303-1310.

[88] M. Tafesse, H.-K. Kim, The role of carbon nanotube on hydration kinetics and shrinkage of cement composite, J Composites Part B: Engineering, 169 (2019) 55-64.

[89] M. Mahinroosta, A. Allahverdi, A Scoping Review on Integrating Inorganic Nanomaterials into Cement Composites, Advances in Civil Engineering Materials, 8 (2019) 526-553.

[90] D. Shafaei, S. Yang, L. Berlouis, J. Minto, Multiscale pore structure analysis of nano titanium dioxide cement mortar composite, Materials Today Communications, 22 (2020) 100779.

[91] K. Sing, D. Everett, R. Haul, L. Moscou, R. Pierotti, J. Rouquerol, T.J.P.A.C. Siemieniewska, International union of pure and applied chemistry, IUPAC, 57 (1985) 603.

[92] W. Meng, K.H. Khayat, Effect of graphite nanoplatelets and carbon nanofibers on rheology, hydration, shrinkage, mechanical properties, and microstructure of UHPC, Cem. Concr. Res., 105 (2018) 64-71.

[93] A. Engbert, J. Plank, Impact of sand and filler materials on the hydration behavior of calcium aluminate cement, Journal of the American Ceramic Society, 104 (2021) 1067-1075.

[94] Y. Reches, K. Thomson, M. Helbing, D.S. Kosson, F. Sanchez, Agglomeration and reactivity of nanoparticles of SiO2, TiO2, Al2O3, Fe2O3, and clays in cement pastes and effects on compressive strength at ambient and elevated temperatures, Construction Building Materials, 167 (2018) 860-873.

[95] A. Hawreen, J.A. Bogas, A.P.S. Dias, On the mechanical and shrinkage behavior of cement mortars reinforced with carbon nanotubes, Construction and Building Materials, 168 (2018) 459-470.

[96] J. Young, Physical mechanisms and their mathematical descriptions, J Mathematical modeling of creep, (1988) 63-98.

[97] X. Liu, T. Fang, J. Zuo, Effect of Nano-Materials on Autogenous Shrinkage Properties of Cement Based Materials, Symmetry, 11 (2019) 1144.

Appendix

Free drying shrinkage tests for the seven mixtures used in this study.

Batch # 1 (Control)			Casting date: 11/21/2020							
Age (days)	Date	Time of the test	Temprture (C)	RH (%)	Ref. Bar (in)	Change (in) Spe.1	Change (in) Spe.2	Shr. 1 (%)	Shr. 2 (%)	Ave.Shr. (%)
0	11/21/2020									
2	11/23/2020	5:30:00 PM	22 ± 4	30	0.1	0.0478	0.0455			
3	11/24/2020	6:51:00 PM		26.6	0.1	0.055	0.053			
5	11/26/2020	5:44:00 PM		32.8	0.1	0.0529	0.0501	-0.021	-0.029	-0.025
7	11/28/2020	6:00:00 PM		28.1	0.1	0.0508	0.0479	-0.042	-0.051	-0.0465
14	12/5/2020	5:45:00 PM		29.2	0.1	0.0495	0.0481	-0.055	-0.049	-0.052
28	12/20/2020	8:35:00 PM		32	0.1	0.0489	0.0474	-0.061	-0.056	-0.0585
56	1/17/2020	7:05:00 PM		27.3	0.1	0.0483	0.047	-0.067	-0.06	-0.0635

Batch # 2 (CNFs-0.25)			Casting date: 11/22/2020							
Age (days)	Date	Time of the test	Temprture (C)	RH (%)	Ref. Bar (in)	Change (in) Spe.1	Change (in) Spe.2	Shr. 1 (%)	Shr. 2 (%)	Ave.Shr. (%)
0	11/22/2020									
2	11/24/2020	6:16:00 PM	22 ± 4	28.5	0.1	0.061	0.06			
3	11/25/2020	6:00:00 PM		27.4	0.1	0.0658	0.062			
5	11/27/2020	6:10:00 PM		30.9	0.1	0.065	0.0589	-0.008	-0.031	-0.0195
7	11/29/2020	6:25:00 PM		25.6	0.1	0.0636	0.058	-0.022	-0.04	-0.031
14	12/6/2020	7:31:00 PM		30	0.1	0.063	0.0575	-0.028	-0.045	-0.0365
28	12/21/2020	5:01:00 PM		28.8	0.1	0.0625	0.0569	-0.033	-0.051	-0.042
56	1/18/2020	7:45:00 PM		27	0.1	0.0616	0.056	-0.042	-0.06	-0.051

Batch # 3 (CNFs-0.5)			Casting date: 11/22/2020							
Age (days)	Date	Time of the test	Temprture (C)	RH (%)	Ref. Bar (in)	Change (in) Spe.1	Change (in) Spe.2	Shr. 1 (%)	Shr. 2 (%)	Ave.Shr. (%)
0	11/22/2020									
2	11/24/2020	6:20:00 PM	22 ± 4	28.5	0.1	0.055	0.058			
3	11/25/2020	6:10:00 PM		27.4	0.1	0.0608	0.062	0	0	0
5	11/27/2020	6:39:00 PM		30.9	0.1	0.0579	0.0601	-0.029	-0.019	-0.024
7	11/29/2020	6:30:00 PM		25.6	0.1	0.0558	0.0598	-0.05	-0.022	-0.036
14	12/6/2020	7:40:00 PM		30	0.1	0.0552	0.0592	-0.056	-0.028	-0.042
28	12/21/2020	5:10:00 PM		28.8	0.1	0.0548	0.0586	-0.06	-0.034	-0.047
56	1/18/2020	7:52:00 PM		27	0.1	0.0542	0.0577	-0.066	-0.043	-0.0545

Batch # 4 (Al_2O_3/CNFs-0.25)						Casting date: 11/28/2020				
Age (days)	Date	Time of the test	Temprture (C)	RH (%)	Ref. Bar (in)	Change (in) Spe.1	Change (in) Spe.2	Shr. 1 (%)	Shr. 2 (%)	Ave.Shr. (%)
0	11/28/2020									
2	11/30/2020	6:50:00 PM	22 ± 4	25.6	0.1	0.0647	0.0622			
3	12/1/2020	7:20:00 PM		33.6	0.1	0.067	0.066	0	0	0
5	12/3/2020	7:05:00 PM		25.6	0.1	0.0649	0.0638	-0.021	-0.022	-0.0215
7	12/5/2020	5:45:00 PM		29.2	0.1	0.0647	0.0634	-0.023	-0.026	-0.0245
14	12/12/2020	6:33:00 PM		31.3	0.1	0.064	0.0624	-0.03	-0.036	-0.033
28	12/26/2020	5:37:00 PM		28	0.1	0.0635	0.0615	-0.035	-0.045	-0.04
56	1/23/2020	4:30:00 PM		29.6	0.1	0.0625	0.0612	-0.045	-0.048	-0.0465

Batch # 5 (Al_2O_3/CNFs-0.5)						Casting date: 11/28/2020				
Age (days)	Date	Time of the test	Temprture (C)	RH (%)	Ref. Bar (in)	Change (in) Spe.1	Change (in) Spe.2	Shr. 1 (%)	Shr. 2 (%)	Ave.Shr. (%)
0	11/28/2020									
2	11/30/2020	7:00:00 PM	22 ± 4	25.6	0.1	0.0598	0.0583			
3	12/1/2020	7:34:00 PM		33.6	0.1	0.0634	0.0616	0	0	0
5	12/3/2020	7:15:00 PM		25.6	0.1	0.0619	0.0582	-0.015	-0.034	-0.0245
7	12/5/2020	5:58:00 PM		29.2	0.1	0.0607	0.0578	-0.027	-0.038	-0.0325
14	12/12/2020	6:42:00 PM		31.3	0.1	0.0598	0.0575	-0.036	-0.041	-0.0385
28	12/26/2020	5:55:00 PM		28	0.1	0.0588	0.057	-0.046	-0.046	-0.046
56	1/23/2020	4:48:00 PM		29.6	0.1	0.058	0.0565	-0.054	-0.051	-0.0525

Batch # 6 (CNFs-0.125)						Casting date: 11/30/2020				
Age (days)	Date	Time of the test	Temprture (C)	RH (%)	Ref. Bar (in)	Change (in) Spe.1	Change (in) Spe.2	Shr. 1 (%)	Shr. 2 (%)	Ave.Shr. (%)
0	11/30/2020									
2	12/2/2020	5:45:00 PM	22 ± 4	30	0.1	0.0585	0.0483			
3	12/3/2020	6:35:00 PM		25.6	0.1	0.0592	0.0515			
5	12/5/2020	5:21:00 PM		29.2	0.1	0.0559	0.0503	-0.033	-0.012	-0.0225
7	12/7/2020	8:18:00 PM		31.7	0.1	0.055	0.0482	-0.042	-0.033	-0.0375
14	12/13/2020	5:43:00 PM		27.3	0.1	0.0547	0.0479	-0.045	-0.036	-0.0405
28	12/29/2020	5:37:00 PM		28	0.1	0.0545	0.0473	-0.047	-0.042	-0.0445
56	1/26/2020	4:54:00 PM		26.5	0.1	0.0534	0.0466	-0.058	-0.049	-0.0535

Batch # 7 (Al_2O_3/CNF-0.125)						Casting date: 11/30/2020				
Age (days)	Date	Time of the test	Temprture (C)	RH (%)	Ref. Bar (in)	Change (in) Spe.1	Change (in) Spe.2	Shr. 1 (%)	Shr. 2 (%)	Ave.Shr. (%)
0	11/30/2020									
2	12/2/2020	6:10:00 PM	22 ± 4	30	0.1	0.0598	0.0628			
3	12/3/2020	6:46:00 PM		25.6	0.1	0.0618	0.0644	0	0	0
5	12/5/2020	5:44:00 PM		29.2	0.1	0.0601	0.0634	-0.017	-0.01	-0.0135
8	12/8/2020	8:30:00 PM		31.7	0.1	0.0598	0.0629	-0.02	-0.015	-0.0175
14	12/13/2020	5:53:00 PM		27.3	0.1	0.059	0.062	-0.028	-0.024	-0.026
28	12/29/2020	5:54:00 PM		28	0.1	0.0586	0.0605	-0.032	-0.039	-0.0355
56	1/26/2020	5:05:00 PM		26.5	0.1	0.0581	0.06	-0.037	-0.044	-0.0405